# Optimization of Laser-Sintered 3D Direct Laser-Written Optomechanical Resonators

Sinja Elea Voss

Bachelorarbeit in Physik
angefertigt im Institut für Angewandte Physik

vorgelegt der
Mathematisch-Naturwissenschaftlichen Fakultät
der
Rheinischen Friedrich-Wilhelms-Universität
Bonn

August 2025

Ich versichere, dass ich diese Arbeit selbstständig verfasst und keine anderen als die angegebenen Quellen und Hilfsmittel benutzt sowie die Zitate kenntlich gemacht habe.

Bonn, 27.08.2025. .....

Datum Unterschrift

1. Gutachter: Prof. Dr. Sebastian Hofferberth
2. Gutachter: Prof. Dr. Stefan Linden

# Acknowledgements

I am deeply grateful to Prof. Dr. Sebastian Hofferberth for the opportunity to work on this project in the NQO group, as well as for both challenging and guiding me throughout this work. I would also like to thank Prof. Dr. Stefan Linden for kindly serving as the second examiner of this thesis.

I would like to express my sincere gratitude to the entire FCO office for always being available for discussions, providing valuable information, and actively thinking along with me on the challenges I encountered during this project. I am especially thankful for the guidance and support from Lukas and Daniel; I truly could not have asked for more.

Many thanks to Hannes for his encouragement and creative ideas. I would like to thank Paul and Gian-Marco for their support in the fiber lab, and Yevgen for helpful advice in chemistry. I also appreciated the coffee breaks and occasional input from David. Special thanks go to Johanna, who previously worked on this project and kindly answered many of my specific questions.

Finally, I would like to thank my family and friends for their emotional support and for helping me by proofreading this thesis.

# Contents

CHAPTER 1

# Introduction

Cavity optomechanics describes the interaction between a mechanical resonator and an optical cavity mode, which originates from the radiation pressure of photons. Moreover, inside a cavity, stronger intensities of light may be reached due to constructive interference in the resonant driving case [1]. This interaction can manifest as noise, for example in gravitational wave detectors such as the interferometer LIGO [2], but it is also an intriguing research topic in fundamental physics, such as quantum limited sensing of mass and force [3] and furthermore, potentially enabling applications in quantum information transfer systems [4].

The FCO (Fiber Cavity Optomechanics) Laboratory uses a membrane-in-the-middle (MIM) system, in which a mechanical membrane resonator is integrated into an optical micro cavity. Here, the cavities partially consist of the mirror-coated end facets of optical fibers, which enables the realization of small cavity lengths [5]. The membranes are fabricated directly onto a mirror using a commerical 3D direct laser writing system (Nanoscribe PPGT+) and serve as micro-mechanical oscillators [6]. This fabrication technique allows for great flexibility and straight-forward integration. A high mechanical quality factor is required for most optomechanics applications. The $Q$-factor describes how well the energy introduced into the system remains within the system, in other words, it characterizes the system's losses.

The $Q$-factor is defined as

$$Q = \frac{\omega_r}{\Delta\omega_r},$$

where $\omega_r$ is the resonance frequency and $\Delta\omega_r$ is the linewidth of the resonance. The conventional polymer-based resist materials in 3D direct laser writing, like IP-S by Nanoscribe, which is mainly used in the FCO-Laboratory to print the membranes, only have an internal Q-factor of typically $\sim 20$ [7]. The goal is to enhance the mechanical quality of the 3D-printed micromechanical oscillators. This can be achieved, for example, by increasing the strain in the membranes and engineering the mechanical system making use of so-called dissipation dilution [8]. Since IP-S is a polymer-based material, the intrinsic losses are quite large [9] compared to standard MIM materials such as Silicon Nitride [10]. For this reason, it is interesting to explore printing with a different material.

A good candidate is silica (quartz glass) as silica-based state of the art micromechanical oscillators feature very low damping with $Q$-factors up to $2 \times 10^8$ at room temperature [11]. Since pure silica cannot be directly printed, this thesis, which is a follow-up to a previous BSc project by J. Stein from 2025 [12], aims to further investigate the fabrication of micro-membranes using GP-Silica to enlarge the $Q$-factor. GP-Silica is another resin by Nanoscribe, that, in addition to monomers and photoinitiators, contains roughly 40% [12] silica particles. Usually, the printed GP-Silica structures are debinded and sintered in a vacuum oven at temperatures up to 1300 °C, to turn the printed structures into pure amorphous silica glass. It is expected, that, in this process step, the structures will decrease in size by up to 30 % [13]. However, the mirrors that form the cavity and serve as substrates for the membranes cannot withstand these high temperatures. Therefore, in this work, the debinding and sintering of the GP–Silica are performed using a $CO_2$ laser, which is normally used to ablate a dimple on a fiber end facet for manufacturing concave fiber mirrors [14]. An open experimental challenge is finding suitable parameters in order to identify the

threshold, at which the membranes are fully sintered while preserving their geometry.

This thesis is structured as follows: In Chapter 2, a brief overview of the general work process and the results of the previous thesis on this topic, i.e., the status quo, is provided. Then, the results and complications encountered in reproducing the previous results are described. Subsequently, in Chapter 3, attention is directed toward measuring the optical quality of GP–Silica cubes. Finally, the emphasis is placed on the further development and fabrication of GP–Silica membranes in Chapter 4.

CHAPTER 2

# Experimental setups used and reproduction of previous results

This thesis builds upon previous work done in our research group [12], which explored 3D direct laser writing micrometer scale membranes with the novel GP-Silica resin as a proof of principle experiment. GP-Silica was developed by Nanoscribe for printing structures with volumes of 1-400 $mm^3$ [15], but for this application, we want to obtain membranes with volumes of $0.1 mm^3$ or less as we want to integrate them into fiber-based microcavities.

In the previous work, it was shown that it is possible to print first GP-Silica membranes with limited structural definition using the 63× objective of the Nanoscribe. Furthermore, first attempts of sintering the membranes with a $CO_2$ laser were made to replace the standard sintering process with a vacuum oven. However, the thesis also expressed that the optimal parameters for proper sintering of the membranes still need to be found, which is further discussed in Chapter 4.

First, the relevant setups for this thesis are briefly introduced in Section 2.1. Following this in Section 2.2, the reproduction and investigation of the previous results is presented. Here, the effects of the ageing of the resin are discussed. Finally, the process of coating GP-Silica on a sample for further testing of sintering parameters without having to print structures is described in Section 2.3.

## 2.1 Overview of employed experimental setups and devices

The first step in the fabrication of the membranes is to print them using 3D direct laser writing with the commercial Nanoscribe PPGT+ system. The polymerization of the resin occurs through two-photon absorption. As only the localalized volume where two photons simultaneously apply their energy to the material becomes polymerized, it is possible to print objects with sub-micrometer scale resolution [16]. However, the resolution also strongly depends on the resin used as well as on the objective which collimates the laser beam. In this case, the higher resolution 63× Nanoscribe objective [17] is needed, due to the required resolution for the membranes. The usage of this objective in combination with GP Silica has not been characterized by Nanoscribe but is interesting for our application.

The work process is as follows: First, the GP-Silica is applied onto an Indium tin oxide (ITO) coated glass substrate. This is a conductive, transparent material that serves as a substrate for printing, because its refractive index differs sufficiently from the refractive index of the resin, which ensures that the interface of the substrate gets found by the integrated *Interface-finder* [18]. The structures are then printed in the Dip-in Laser Lithography (DiLL) mode, where the substrate is flipped upside down, and the objective dips into the resin from underneath (see Figure 2.1). The required laser path for the printing process of the structures is programmed in *DeScribe*, a software provided by Nanoscribe, which then generates a `.gwl` file that is read by the printer. After printing the structures, they need to get developed to remove the unpolymerised liquid resin and subsequently debinded and sintered. In GP-Silica, the binder holding the glass particles together consists of free-radical-polymerized methacrylate/acrylate molecules. During the thermal debinding process, the binder undergoes pyrolysis due to the increased temperature, meaning that

the large polymer chains are split into smaller, volatile components. The aim is to completely remove the binder while preserving the structure of the sample. At temperatures of 1000 °C and higher, the sintering process begins. In the sintering process, the high surface energy of the glass particles gets decreased through atomic diffusion and particle deformation. Due to the atomic diffusion the particles form bonds, the density increases, porosity decreases and the material ultimately becomes a solid body [19]. For further information on the general work-flow for printing with GP-silica see the Bachelor thesis of Johanna Stein [12] from our experimental group.

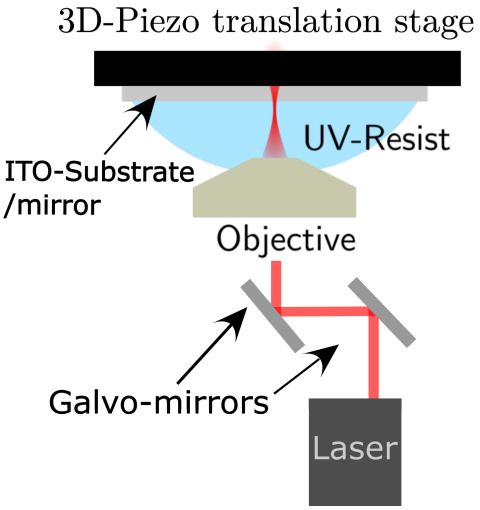


Figure 2.1: Schematic representation of the DiLL printing method. The laser beam is collimated through the objective, which is dipped into the UV-resist (here GP–silica resin). The resist is applied onto the ITO substrate or a mirror. The substrate is moved in the $z$-direction using the piezo stage, while the $x$–$y$ plane is accessed by adjusting the laser beam path, via adjustable galvo mirrors. Figure adapted from [6].

For the sintering process a $CO_2$ laser setup, also referred to as shooting setup due to its primary use case for shooting the laser on fibers for fiber mirror production, is used, which can be seen in Figure 2.2. The sample gets mounted onto a 3D stage with a sample holder, which allows adjustment of the sample into the focal point of the interferometer. For shooting, the sample is moved into the laser beam path, where the distance to the focal point of the laser beam is referred to as $y_{\text{diff}}$. The shooting setup contains an acousto-optic modulator (AOM), which modulates the used laser power from the $1^{st}$ order of the $CO_2$ laser. The power of the $0^{\text{th}}$ order is continously monitored with a photodiode. Calibration measurements of this laser power in relation to the AOM voltage are carried out with a power meter (PM) at the end of the laser path. The setup is controlled via a Python script, which allows for adjustment of various parameters. This is further detailed in Chapter 3. The adjustment of the samples into the shooting setup can be seen in Figure 2.3. For more in-depth information on the shooting setup refer to the Master thesis of Moritz Scharfstaedt [14] and for more details on the mounting of the substrate into the setup refer to Stein [12].

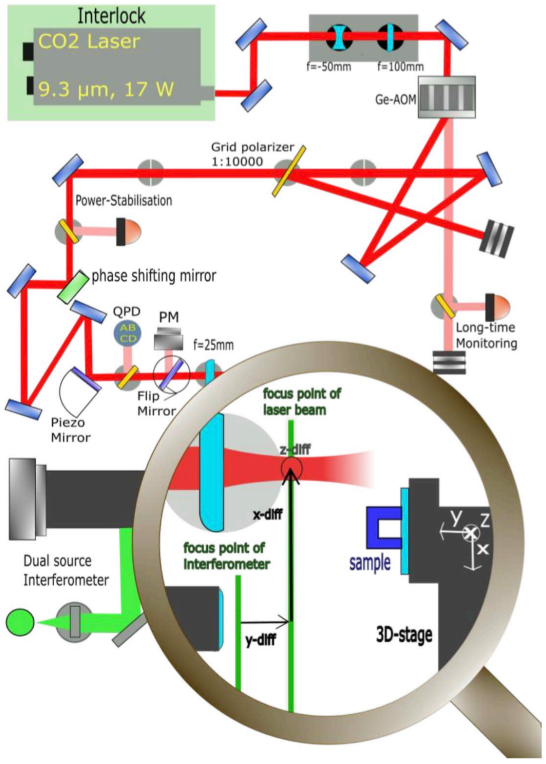


Figure 2.2: Schematic model of the shooting setup, including all components. The $CO_2$ laser is first collimated and then directed to the AOM, which redirects the $1^{st}$ order of the laser beam to the sample area, while the $0^{th}$order is contiously monitored on a photodiode. Before the focus point of the laser beam, a flip mount is integrated, allowing the beam to be deflected to a power meter, which serves as a calibration device for the needed AOM voltage. The dual-source interferometer, containing a camera to observe and adjust the samples, is shown at the bottom of the schematic model, along with the sample attached to the 3D stage. Taken from [12].

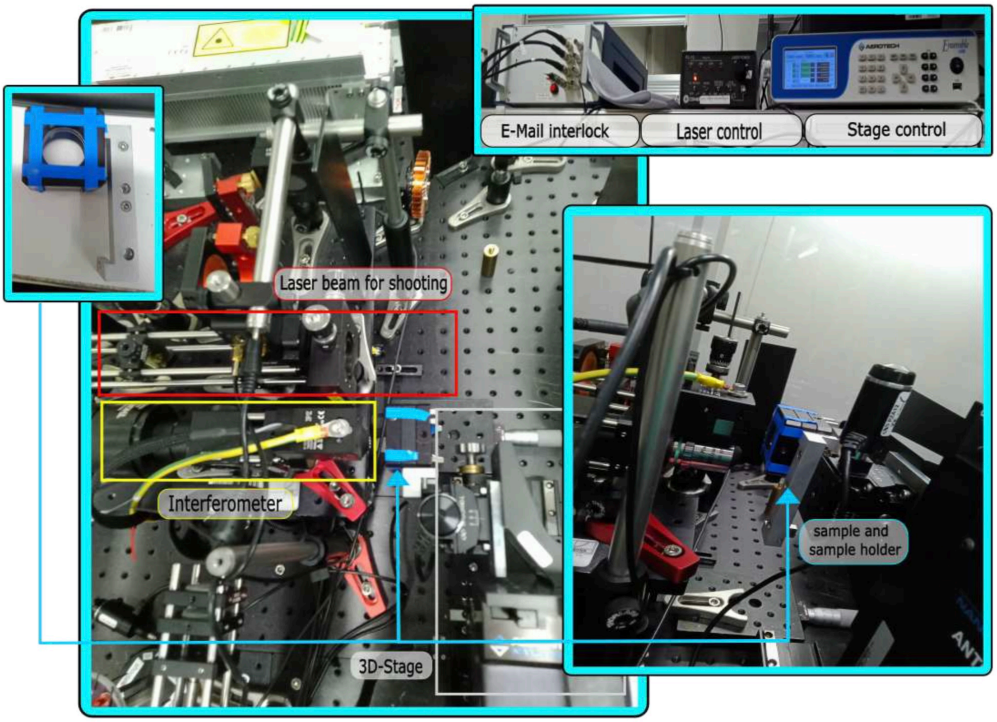


Figure 2.3: Image of the shooting setup as seen from above with the location of the interferometer, 3D stage, sample, and the laser beam visible in the center. The taped sample mounted onto the sample holder is shown in the picture on the top left. The devices used to control the laser and the stage are displayed at the top right, while on the bottom right, the built-in sample is shown. Taken from [12].

## 2.2 Reproducing previous results

The first step of this thesis was to reproduce the previous results. First attempts with the exact same process and the same printing parameters, which will be further discussed in Chapter 3, led to very similar looking results (see Figure 2.4). To obtain reliable shooting parameters, it is necessary to print a significantly larger amount of membranes. However, while printing more membranes, it became evident that the resin developed major defects, which can be seen in Figure 2.5. Over time, the resolution of the prints deteriorated progressively. This behavior can be interpreted as the resin exceeding its shelf life, which is given as three months [13] after opening the cartridge. At that point, the resin used was six months old. These results show that GP-silica is very sensitive compared to IP-S, because IP-S can be used long after its expiration date.

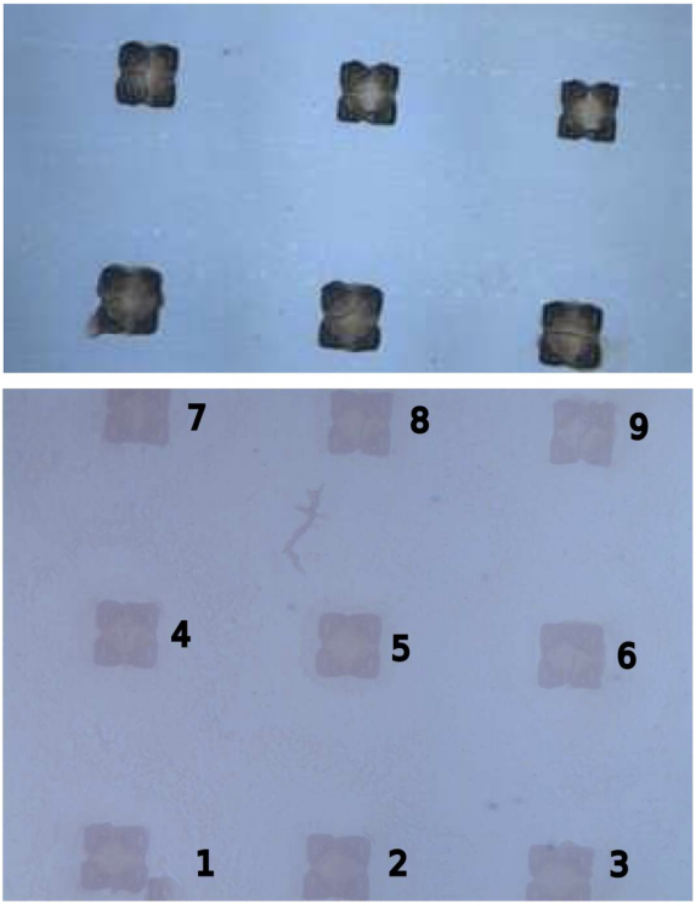


(a)

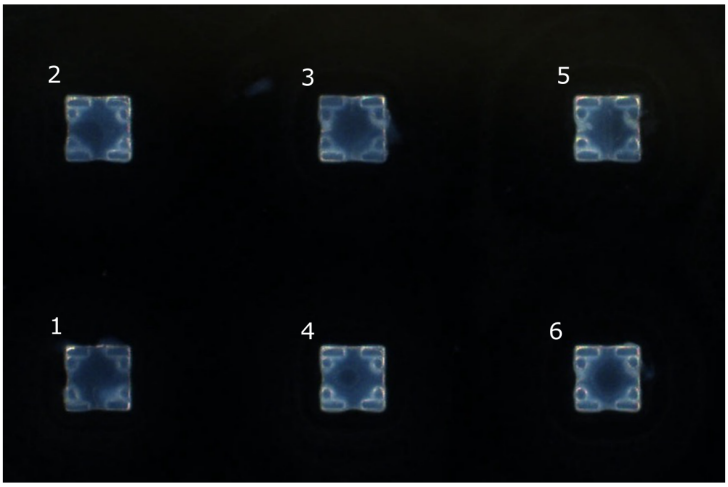


(b)

Figure 2.4: Comparison of previous printing results and the first reproduction attempt with the same parameters. (a) Best previous printing results [12]. The pictures were taken with a light microscope in bright-field mode at low resolution. A rough assessment of the quality indicates that there are no significant leakages or cracks in the membranes. (b) First print with previous best printing parameters for this geometry. The membranes appear to be free of cracks, air bubbles, and leakages, and exhibit well-defined edges. The picture was taken with the same light microscope in dark-field mode (further information on the different light modes is given in Chapter 4).

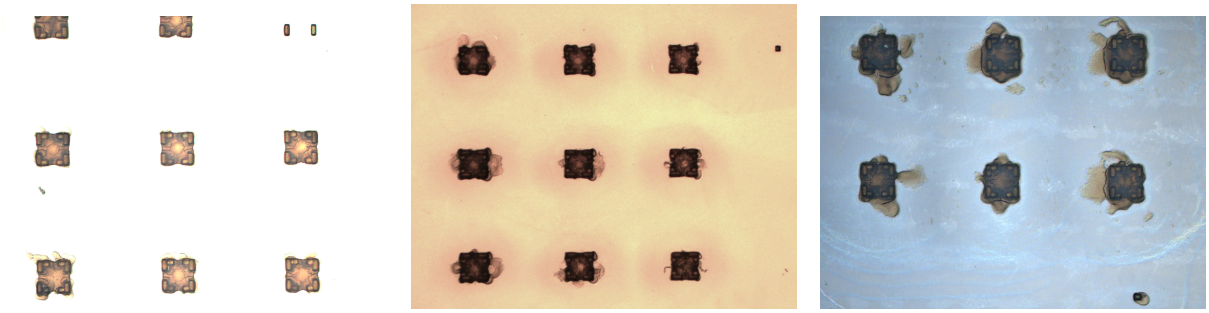

Figure 2.5: Three membrane array prints with the same geometry from the previous results and similar printing parameters are shown. The prints, displayed from left to right, were produced over a one-month period. The degradation of the resin due to aging is evident. It is noticeable that the quality decreases significantly and that the occurrence of leakages increases.

## 2.3 Coating-stage-set-up

Due to these issues, it was not possible to obtain reliable shooting parameters when working with the inhomogeneous and non-reproducible membranes printed with expired GP-Silica. Therefore, instead of printing membranes directly onto the substrate, it was attempted to fully coat the ITO substrates with GP-Silica in order to create a larger polymerized area for shooting experiments, potentially leading to parameters applicable to membranes in the future. However, for conventional spin coating, GP-Silica is not suitable and must therefore be applied manually. GP-Silica exhibits shear-thickening behavior [20]. Thus, although it is less viscous than other resins, it still appears viscous when being spread. As a result, the resin forms stripes and shows different mechanical characteristics when spread in different directions, making GP-Silica overall difficult to handle in any setting other than the normal printing process.

The coating process is carried out with a built setup, which is shown in Figure 2.6. Here, the ITO substrate is fixed onto a 3D stage with tape and the resin is applied directly from the cartridge onto the substrate. To ensure a homogeneous film thickness, a razor blade is attached to a movable pillar, which is also height-adjustable. The blade is lowered to the desired thickness, and the pillar is then slowly moved so that the razor blade brushes over the drop of resin. In addition to the mentioned shear forces, surface tension and the rapid reaction of GP-Silica with air [20], which hardens the resin, make achieving a uniform coating challenging with this method. As an alternative to curing GP-Silica with the Nanoscribe, it can be polymerized directly with an UV lamp, which is more practical for curing a relatively large area. After spreading the resin, the pillar with the attached razor blade is removed, and the UV lamp is placed directly above the substrate.

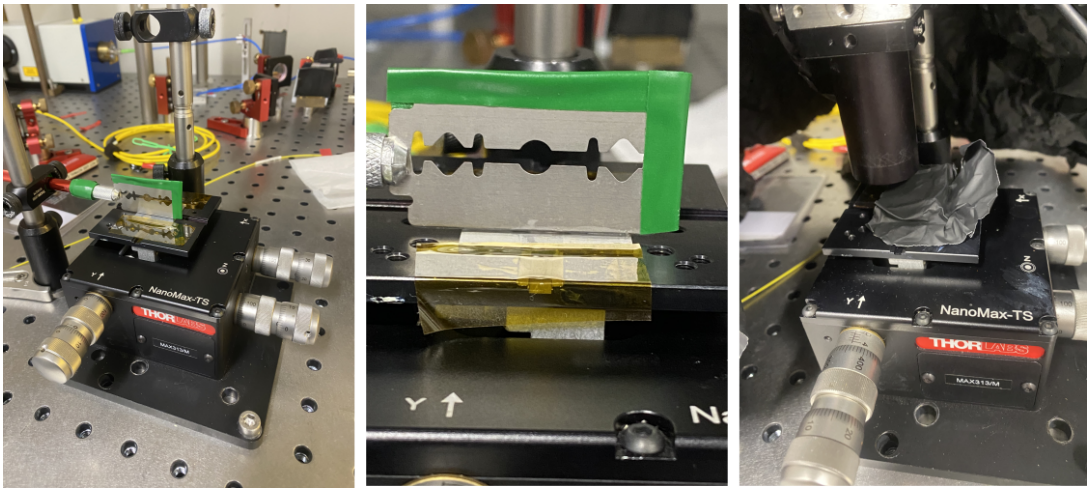


Figure 2.6: Coating-stage setup: *Left*: Spreading of the resin is performed with a razor blade attached to a movable pillar, while the substrate is fixed onto a stage. *Center*: The razor blade is lowered down to the substrate to create the thinnest layers possible (with this setup). *Right*: The pillar is removed and the UV lamp is set up. The black tube, which is directly aimed at the coated substrate (missing in the picture), collimates the UV light. The blackened aluminum foil piece is shaped to function as a mask, shielding the layers that require shorter exposure durations than others.

The major issue is that even when using a razor blade to spread the GP-Silica, the layer remains too thick. It is not possible to reliably reduce the thickness down to a comparable thickness to the printed structures of 2.5–20 $\mu m$ with this method. If the resin layer is too thin (see Figure 2.7(b)), it becomes overexposed and develops cracks (as expected [20]). If the resin layer is thick, cracks still occur under the same exposure conditions as for thinner layers (see Figure 2.7(a)). However, the regions that remain uncracked are larger in comparison to the laser beam expansion and the printed structures.

During the development process, the thicker layers do not adhere well to the substrates potentially because of the increased mass. The printed structures were placed in a methanol bath for ten minutes, followed by an additional minute in fresh methanol, as recommended by Nanoscribe [20] and identical to the procedure used in the previous work. Initially the substrate was placed vertically into the methanol [12]. However, for the thicker layers to adhere to the substrate during development, the sample was instead placed horizontally in the methanol bath. After curing, the GP-Silica gradually turned into a darker yellowish color. The differences in exposure and coloration are shown in Figure 2.8(a), indicating that the curing was successful. In comparison to micrometer-scale structures, the larger coated areas make the varying degrees of curing visible to the naked eye. In Figure 2.8(b), a coated substrate after development is shown. Finally, the GP-Silica layers appear white, which indicates that the layers were properly cured and developed [13]. Although the desired thickness of the coating was not achieved, first variations of shooting parameters could be tested, which is further discussed in Chapter 3.

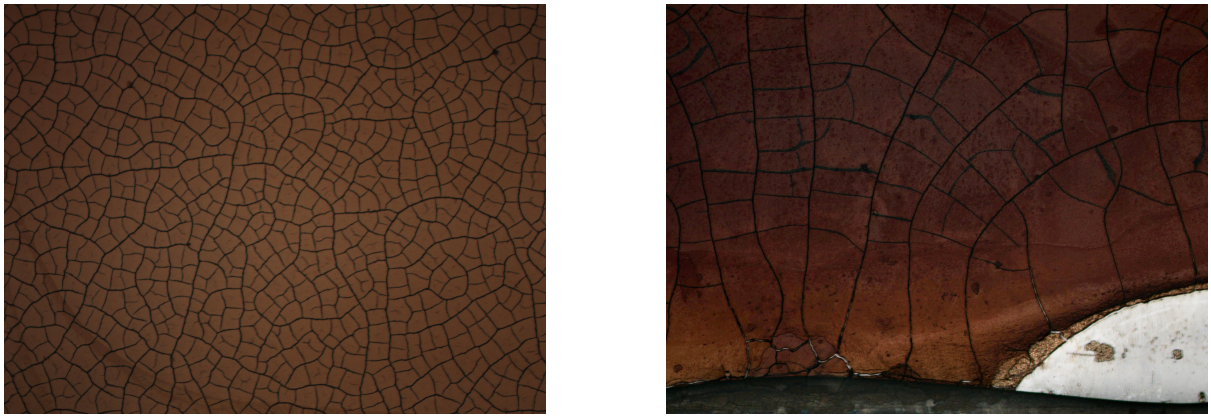

(a) (b)

Figure 2.7: Comparison of two coating thicknesses of possibly overexposed GP-Silica after 15 minutes of exposure to a 4V UV lamp. **(a)** Thinner layer, developed as expected; due to the same exposure duration, it exhibits significantly more cracks than the thicker layer. This coating is not suitable as a sample for testing shooting parameters. **(b)** Thick layer, with cracks potentially caused by overexposure. The uncracked areas are roughly the size of the beam diameter and match the diameter of the printed structures.

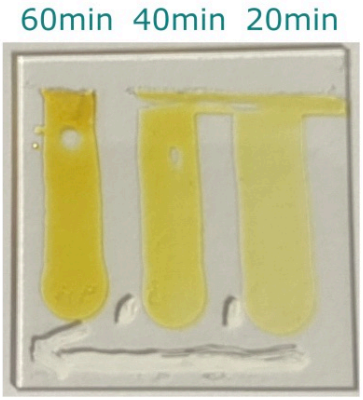


(a) UV-cured coatings with varying exposure durations, using a 5 W (4 V) UV lamp.

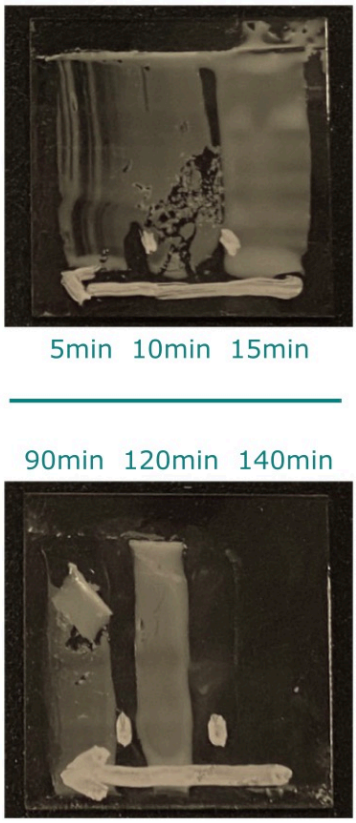


(b) Coatings UV-cured and developed horizontally for 5 min in methanol.

Figure 2.8: **(a)** The results of the coating method are shown. The layers appear coarsely homogeneous to the naked eye, and the yellowish color intensifies with longer curing durations. With larger areas, it may be possible to assess the degree of exposure (under-, right-, or overexposure) based on color. **(b)** The results of developing the coatings with different curing durations are shown. In the bottom images, it is observable that when parts of the coating detach, they do so in patches, which could explain why the entire coating with a curing duration of 140 minutes disappeared. In the top image, thinner layers were attempted; however, they appear inhomogeneous in height, and stripe formation is visible.

CHAPTER 3

# Optical properties of GP-Silica sintered structures

The focus is first placed on the optical properties of sintered GP-Silica in general. As discussed in Chapter 2 the membranes are not optimized yet, and the correct sintering parameters still need to be determined. Before focussing on these membranes in Chapter 4 the problem is simplified first by printing cubes instead, which can be used to investigate the optical properties of GP-Silica. Cubes are easier to print with GP-Silica because they do not require small features and represent an overall simple geometry. Therefore, scaling is also more straightforward with this geometry. The printing duration is shorter, because they do not need to get printed as densely as the membranes and the printing parameters are more flexible. Therefore it is possible to print a larger number of cubes in one array. A short printing duration is important because the quality degenerates after a printing duration of 3 hours [12].

Section 3.1 focuses on determining the optimal printing parameters, while Section 3.2 addresses the determination of the optimal sintering parameters. Finally, Section 3.3 presents a measurement of the finesse using the vacuum fiber microscope (VFM).

## 3.1 Optimizing the printing process (for cubes)

The relevant adjustable printing parameters are primarily the laser power (LP), which is linearly proportional to the applied laser dose, and the writing speed of the laser, also referred to as the scan speed (ScSp), which is particularly important for the stability of the printed structures and additionally determines their exposure duration. The laser is a femtosecond pulsed laser and writes the structures in voxel lines. Voxels are the smallest printable volume. Their size differs, depending on the applied laser dose to the resin and also the material used. The voxel size of GP-Silica is larger than that of other common resins [20]. When preparing a print job, the slicing distance (SD) and hatching distance (HD) are adjustable. The SD is the distance between voxel line layers in the horizontal direction, and the HD, is the vertical distance between voxels. A smaller hatching or slicing distance means that the voxel lines overlap more, resulting in repeated exposures of the resin.

The challenge lies in finding the threshold at which the resin is fully polymerized but not overexposed. As mentioned before in Chapter 2 overexposure leads to the formation of cracks in the printed structures after development. Cubes can be printed with constant printing parameters due to their uniform geometry, which simplifies the process of determining the correct dose and polymerization threshold. The optimal printing parameters can be determined via a dose sweep, where a structure is printed repeatedly in an array while varying different parameters along each axis.

In Figure 3.1, a dose sweep of $50 \times 50\,\mu$m cubes with a height of $2.5\,\mu$m is shown, where the laser power is varied along the x-axis and the scan speed is varied along the y-axis. It is noticeable that the cubes, which were exposed to the lowest laser doses, mostly due to low laser power and, to a lesser extent, high scan speed, did not develop at all. With increased laser doses, the only partially polymerized structures do not exhibit high contrast and appear as faint imprints. It is expected that they are also lower in height, as voxel size increases with higher laser dose. Their edges remain roughly well defined, but this is due to the simple geometry, as opposed to membranes with overhanging features, where the shape

would not be maintained in this underexposed state. Shooting on those underexposed cubes did not show any results, as the "cubes" do not have enough volume to be sintered. The cube with scan speed 5k $\frac{\mu m}{s}$ and laser power 60% is close to the polymerization threshold, at which the print is fully polymerized as intended. The cubes with scan speed ≤ 8k $\frac{\mu m}{s}$ and laser power 90% or 100% are overexposed. The contrast of the edges, observed through the light microscope, increases and a few leakages appear (see cube: 80% LP and 5k $\frac{\mu m}{s}$). With this geometry, even after development, the cubes do not exhibit cracks despite being overexposed, this is probably due to the relatively small volume of the cubes.

After several iterations, in which the cubes were shot at (more on this in Chapter 3.2), it became clear that the best printing parameters are: laser power = 70%, scan speed = 5k $\frac{\mu m}{s}$, slicing distance = 0.18 $\mu m$, hatching distance = 0.08 $\mu m$, with dimensions of 50 × 50 $\mu$m and 2.5 $\mu$m height. These are above the polymerization threshold to ensure that the cubes are high enough to be printed, because the height is initially only 2.5$\mu m$. In the case of a tilted substrate or the voxel sizes being too small, the effective height of the cubes decreases and becomes critical for sintering. This is why the chosen parameters are above the polymerization threshold to ensure that the cubes are tall enough, while remaining well below the dose at which leakages occur. In the following, these printing parameters were therefore used to determine the optimized sintering parameters.

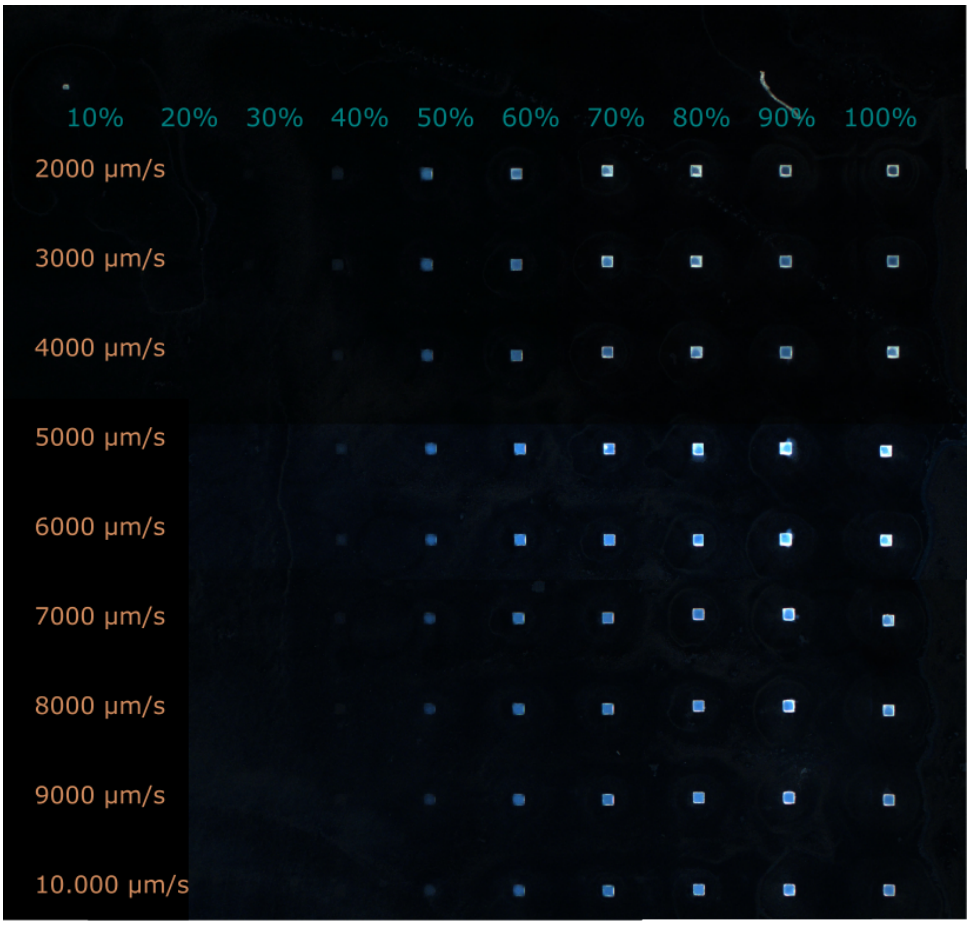


Figure 3.1: Dose variation on cubes with scan speed (vertical axis) ranging from 2000 $\mu$m/s to 10000 $\mu$m/s in increments of 1000 $\mu$m/s, and laser power (horizontal axis) ranging from 10% to 100% in increments of 10%. Laser power scales almost linearly with the dose but exceeds a threshold at which the cubes become overexposed. Scan speed has a slightly smaller influence on the dose, as indicated by the greater variation in quality along the horizontal axis. Underexposed cubes with laser powers below 50% exhibit reduced contrast, whereas overexposed cubes, produced with laser powers of 80% (at 5000 $\mu$m/s or lower scan speed) and higher, display increased contrast and, in some cases, small leakages after development. The extent of the leakages does not seem to scale linearly with increasing dose.

## 3.2 Optimizing the sintering process for printed cubes

The next step is to sinter the printed cubes with the $CO_2$ laser setup, as introduced in Chapter 2. Here, the different parameters of the setup need to be optimized. These parameters include:

- Amount of applied laser pulses $n$
- Power of the pulses $P_0 \cdot a$ (where $P_0$ is the maximum laser power and $a$ is the fraction of maximum power per pulse)
- Duration of the pulses $\tau$
- Delay between pulses $\Delta\tau$
- Relative distance to the laser beam's focal point $y_{\text{diff}}$

As mentioned earlier, a function for varying the laser power profile of a pulse sequence was implemented in the previous thesis on this topic. This lead to initial results as seen in Figure 3.2, supposedly showing more homogeneously sintered membranes as shown in Figure 3.2(a). Without images from the exact same unsintered membrane array under a microscope with identical camera settings, the degree to which the results are sintered is not properly identifiable. Most of the membranes have remained intact but there are no indications that the membranes have shrunk and their transparency has not increased significantly.

In the previous work, a few laser profiles already got tested. Here, the best shooting parameters found were tested with membranes:

- Amount of shots: $n = 10$
- Pulse duration: $\tau = 8\,\text{ms}$
- Pulses-Power profile: $2 \cdot 50\% : 6 \cdot 100\% : 2 \cdot 50\%$
- Maximum power: $P_0 = 0.25\,\text{W}$
- Pulse delay: $\Delta\tau = 100\,\text{ms}$
- Distance: $y_{\text{diff}} = 5.775\,\text{mm}$

This resulted in numerous cases, where the structures either got destroyed or did not get fully sintered. The initially reproduced print job shown in Figure 2.4(b) in Chapter 2 sintered with these parameters using the previous shooting button can be seen in Figure 3.2(b). In Figure 3.2(b)) one can see that the membranes 1 to 3 likely did not get sintered, as there is no shrinkage or more transparency/ color-change in comparison to the images of the unsintered membranes similar to the previous work. While the membranes from 4-6 partially melted and did not kept their inital shape, they appear to have partially turned to glass. In both the bright-field and the dark-field their optical properties have changed. As mentioned before, the goal is to sinter fully while preserving the geometry. It is expected that the structures decrease in size by up to 27 % [20] when being sintered and turned into glass.

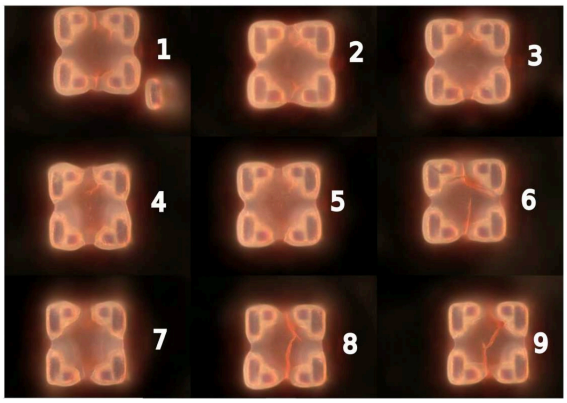


(a)

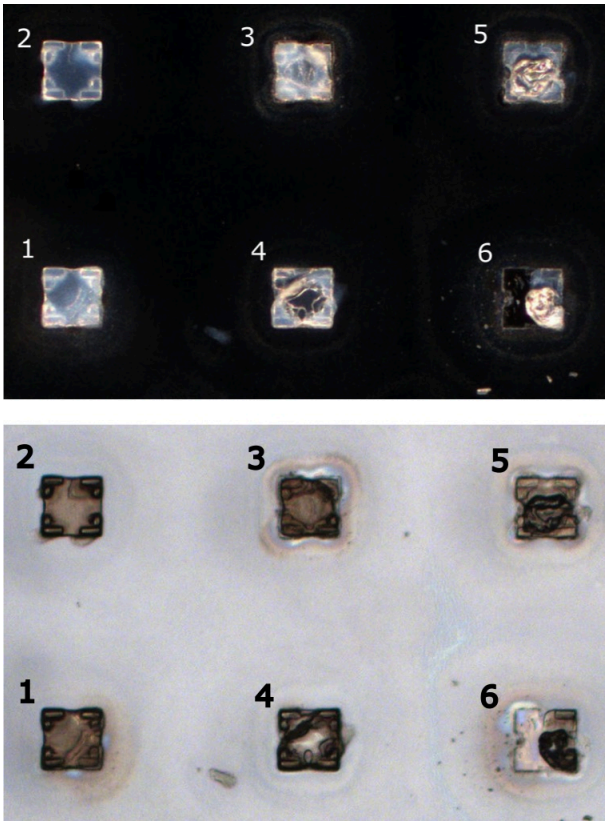


(b)

Figure 3.2: (a) Best sintering results from previous work [12]. There are no indications that the membranes have shrunk and their transparency has not increased significantly. The fact that the center of the membrane appears darker than the outer parts is not a direct indication that the center is now made of glass and rest of the membrane is not. (b) First attempts at sintering with the old shoot button on the first print as seen in dark- (*top*) and bright-field (*bottom*) configuration. The power was increased from 1-6 to 0.15W, 0.20W, 0.25W, 0.30W, 0.40W, 0.50W. The other parameters remained unchanged from the previous ones. Membranes 1-3 were not sintered, although membrane 3 corresponds to the previous shooting parameters. Membrane 4 appears to have partially turned to glass, as its optical properties have changed in both bright- and dark-field. For membranes 5 and 6 the power was too high, so the membranes melted and deformed.

In further testing, which was done to the deficient results, the code exhibited some incomprehensible behavior, such as incorrectly displaying the set pulse delays when plotting the pulse sequence. This likely happened as the shoot button was implemented within a short time during the final phase of the project. Therefore a new more robust shoot-button with the same degree of parameter freedom but enhanced structure was implemented before continuing shooting on structures. In this case, the values

that are put inside the graphical user interface (GUI) match those that are plotted and executed. The

new python code written (see Appendix A.1) creates the laser power profile functions as follows: The function `shoot_button2` creates and starts a laser shoot profile. To realize this, a DAQ card (Data Acquisition-card) is used to define three tasks:

```
- \texttt{analogue\_task}, responsible for controlling the voltage output to the AOM,
which in turn modulates the laser power. \texttt{analogue\_task.ao\_channels...\ }
sets the analog output channel that controls the AOM voltage.

- \texttt{trig\_task}, which generates a single digital pulse functioning as the start
 trigger.

- \texttt{gate\_task}, which produces a digital pulse sequence for gating, which
enables and disables the laser output.
```

Together the counter output channels in `trig_task.co_channels...` and `gate_task.co_channels...` define square wave signals used for triggering and gating. These two digital channels are synchronized to the trigger source. Following that, the variable `self.samples_per_second` determines how many voltage values are generated per second, therefore defining the temporal resolution of the voltage curve, which is limited by the capabilities of the DAQ card (Daq PCI card, input: rate- 250k samples/s, output: rate- 840k sampels per channel). In this case, a sampling rate of 500 kHz was used to obtain relatively high resolution. Going beyond that is not necessary, as a moderate slope may even be beneficial for this application. In the usual debinding and sintering process with an oven, the temperature is also continously adjusted. Then a list `fraction_list = [...]` gets created, which contains fractions of the total laser power that are used for each individual pulse. This part of the function defines the shape of the profile created by the pulses to mimic the temperature curve of the oven. The variables `length_of_a_high` and `length_of_a_low` define the temporal duration (as amount of samples) of each "high" (laser on, scaled by the fraction) and "low" (laser off) segment. The duration of the lows corresponds to the delay between pulses, which can be defined in the GUI, while the duration of the highs depends on the pulse duration, defined via the GUI aswell. After that follows a `for` loop:

```
for fraction in fraction_list:
    print(fraction)
    lows=np.zeros(length_of_a_low)
    highs=np.ones(length_of_a_high)*self.aom.voltage*fraction
    one_pulse=np.concatenate((lows,highs))
    pulses.append(one_puls)
```

In this `for` loop, for each entry in `fraction_list`, a low segment and a scaled high segment are created and concatenated into a single pulse called `one_pulse`. The appending of those pulses results in an array of varying pulse amplitudes. This array then gets concatenated into one continuous voltage profile with:

```
pulses = np.concatenate(pulses, axis=0)
```

To visually monitor the behavior of the shoot button and what the profile looks like, the code includes a plot of the waveform using:

```
plt.plot(pulses[::1000])
```

This plots every 1000th sample for faster rendering. If needed, this interval can be adjusted for finer resolution at the cost of longer plotting time.To ensure correct synchronization of tasks, the analogue and gate tasks are both triggered by a digital edge trigger defined by:

```
analogue_task.triggers.start_trigger.cfg_dig_edge_start_trig(trigger_source=self.
trig_source)
gate_task.triggers.start_trigger.cfg_dig_edge_start_trig(trigger_source=self.
trig_source)
```

The duration of the laser shots with this shoot button can be significantly longer than those used in the conventional applications of the shooting setup. This is because the partially reduced power is compensated by longer pulse duration or a higher number of total pulses. Therefore, it is crucial that the program waits for all tasks to finish before proceeding. This is done using:

```
analogue_task.wait_until_done(timeout=WAIT_INFINITELY)
trig_task.wait_until_done(timeout=WAIT_INFINITELY)
```

### 3.2.1 Sintering with the new shoot-button

Initial tests of the new shooting button, using the best previously established parameters, revealed that the applied dose was even less effective for sintering than when using the old shooting button. In conclusion, the shooting parameter ranges vary greatly from the ones with the new shooting button. Therefore completely new shooting parameters need to be found, starting with the cube geometry.

In a cavity, it is necessary to have a planar and even surface of the printed structure so that scattering is reduced and therefore losses are minimized. The laser beam has a conventional Gaussian transversal profile, which results in an uneven surface of the structures. This can be seen in Figure 3.3(a). To get a better result, the sample needs to be placed at a distance from the focal point of the laser, because the focal point is where the Gaussian profile is most well-defined. If the distance between the focus point and the sample is large enough, the Gaussian profile is broadened, and the power distribution is roughly uniform across the finite surface of the sample. Normally, the distribution of the Gaussian beam can be calculated, and thus an optimal distance can be determined. However, this is not easily possible here due to the many variables, such as the variable shooting parameters and the different focusing conditions for each shot. Further information on this topic can be found in [14].

Moving out of the focus, the results already look more even, as shown in Figure 3.3(b). With the interferometer of the shooting setup it is possible to see that the surface is almost flat, as only few interference fringes can be seen on the cube (see Figure 3.4). There is also no noticeable damage to the structure and the surface seemingly lies in one focal plane when observed through a light microscope. It is also noticeable that the expected shrinkage happened, which is a strong indicator that the observed structures now consist of glass.

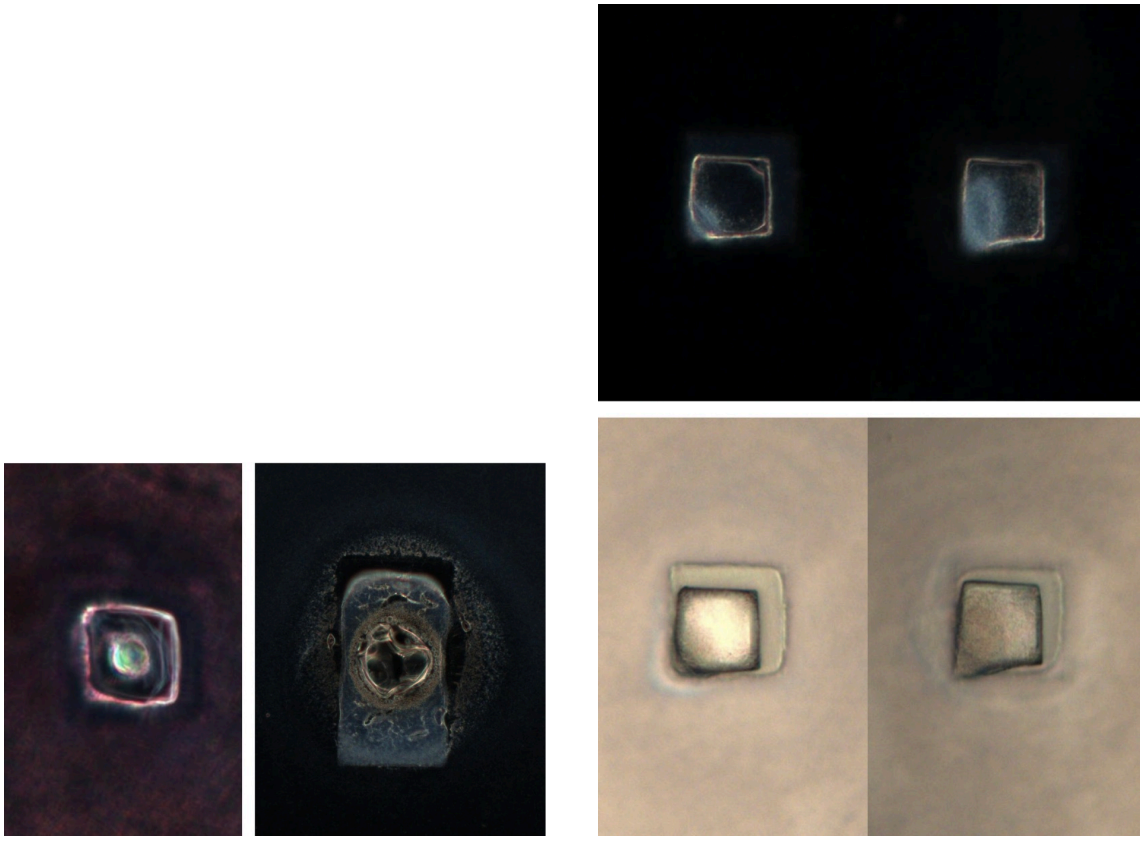

(a) (b)

Figure 3.3: (a) After sintering, the Gaussian profile has been imprinted into the cubes. *Right*: with $\tau = 50\,\text{ms}$, $n = 28$, $P_0 = 0.2\,\text{W}$, Fraction AOM = 0.2:0.3:0.4:1:0.4:0.3:0.2, $\Delta\tau = 100\,\text{ms}$, $y_{\text{diff}} = 5.775\,\text{mm}$. *Left*: with $\tau = 31\,\text{ms}$, $n = 36$, $P_0 = 0.69\,\text{W}$, Fraction AOM = 0.2:0.4:0.6:0.8:1:0.8:0.6:0.4:0.2, $\Delta\tau = 100\,\text{ms}$, $y_{\text{diff}} = 4.2\,\text{mm}$. It can be seen that, even when the distance from the focal point, located at approximately $y_{\text{diff}} = 5.15\,\text{mm}$, is increased, the Gaussian profile is still imprinted if the laser power is too high. (b) Results with the following shooting parameters shown in dark- (*top*) and bright-field (*bottom*): $\tau = 30\,\text{ms}$, $n = 36$, $P_0 = 0.55\,\text{W}$ (*left*) / $0.50\,\text{W}$ (*right*), Fraction AOM = 0.2:0.4:0.6:0.8:1:0.8:0.6:0.4:0.2, $\Delta\tau = 80\,\text{ms}$, $y_{\text{diff}} = 4.2\,\text{mm}$. No imprinted Gaussian profile is visible, and the surfaces appear relatively uniform. However, it can be observed that the cubes are drawn toward one corner, and in these regions they are not uniformly sintered or potentially not sintered at all.

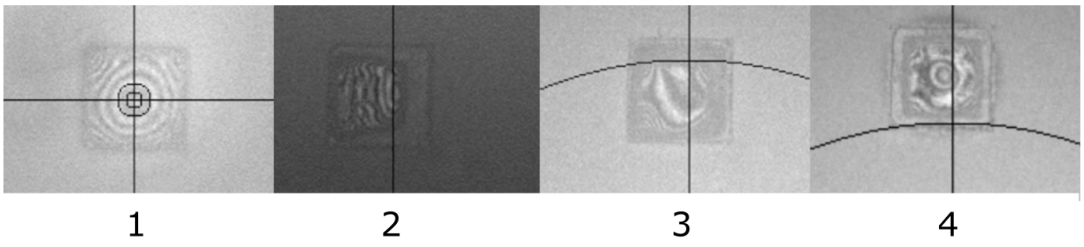


Figure 3.4: Different cubes as seen in the interference microscope of the shooting setup: 1: Unsintered cube, 2: Sintered shrunken cube, 3: Potentionally melted cube with smoothed surface, 4: Cube, which got shot with too much power, therefore there are circular and concentric fringes visible from the imprinted gaussian intensity distribution

The best shooting parameters found for the cubes with a height of 2.5 µm are:

- Pulse duration: $\tau = 30\,\text{ms}$

- Number of shots: $n = 36$
- Laser power profile (AOM fractions): $0.2 : 0.4 : 0.6 : 0.8 : 1 : 0.8 : 0.6 : 0.4 : 0.2$
- Maximum power: $P_0 = 0.6\,\mathrm{W}$
- Pulse delay: $\Delta\tau = 80\,\mathrm{ms}$
- Vertical offset: $y_{\mathrm{diff}} = 4.2\,\mathrm{mm}$

The chosen profile is derived from the fast sintering process with an oven [15], which is recommended for micronsized structures (see Figure 3.5). The transferability is questionable, because the reached temperature to which the structures get exposed to, depends on all of the shooting parameters, and the profile only describes the applied laser power curve. Furthermore, the timescales are extremely different. The rapid sintering process with the oven takes $\sim$ 18 hours, while one shooting sequence takes approximately 1.5 minutes. Nevertheless, this approach provides an additional degree of freedom, which is potentially beneficial for sintering, which requires high temperature precision.

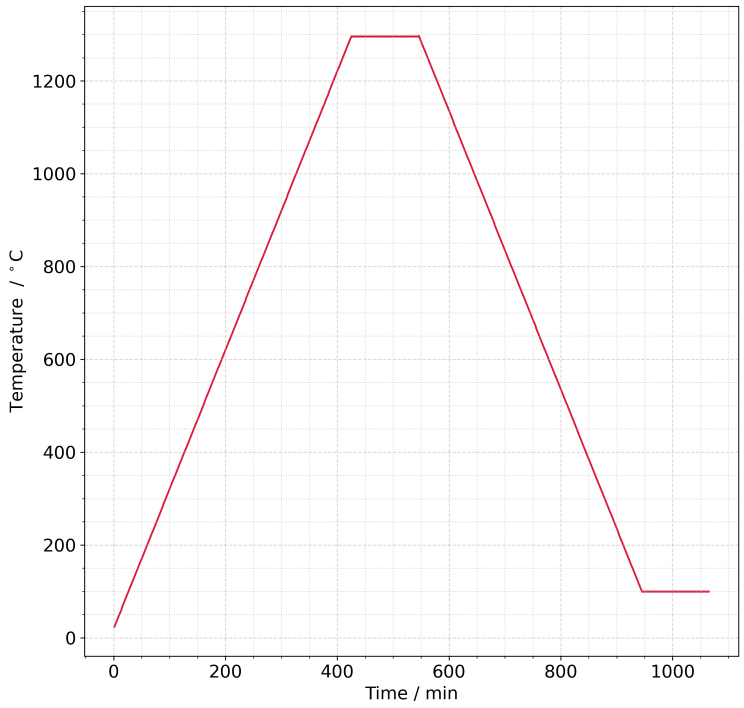


Figure 3.5: Temperature of the GP-Silica fast thermal processing program against time [20].

With the best shooting parameters for $50 \times 50\,\mu$m cubes with a height of $2.5\,\mu$m, the following arrays showed that, while the goals of structure retention, a flat surface and sintered results are met, there still seems to be a thin layer of unsintered resin residue. These layers have different optical properties, which can be seen in Figure 3.6. The potentially non-sintered layer is not transparent and exhibits a higher contrast, particularly in dark-field mode. A possible explanation is that this occurs because the very last layer is in direct contact with the substrate, which could lead to a different thermal behaviour.

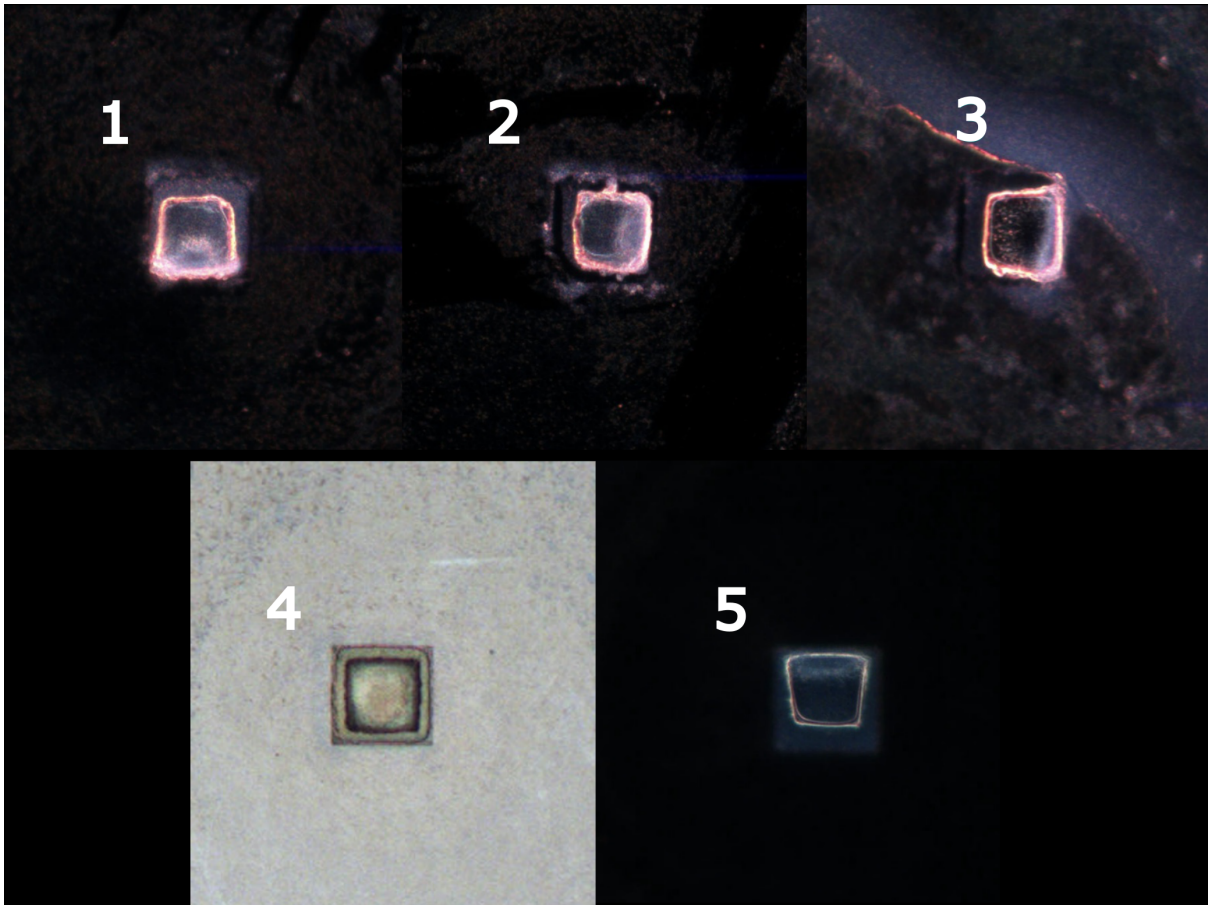


Figure 3.6: Sintered cubes on different substrates. 1-3 are cubes that were printed on a mirror. Comparing 1-3, it seems that the degree of transparency of the shrunken cube depends on the differently colored layer, which is the same size as the cubes were before sintering. 4 and 5 are cubes that were printed on ITO substrate. Here, too, the layer has a different contrast and has the same dimensions as the unsintered cube.

To try to fully sinter the cubes, including the lowermost layer, the laser power was even further increased for the following samples. The results can be seen in Figure 3.7. With a slightly increased dose, the cubes did not keep their shape, deformed, partially melted, and became spherical. The potentially unsintered layer exists partially even in this state. Inside a cavity this last layer would affect the optical finesse of the structure.

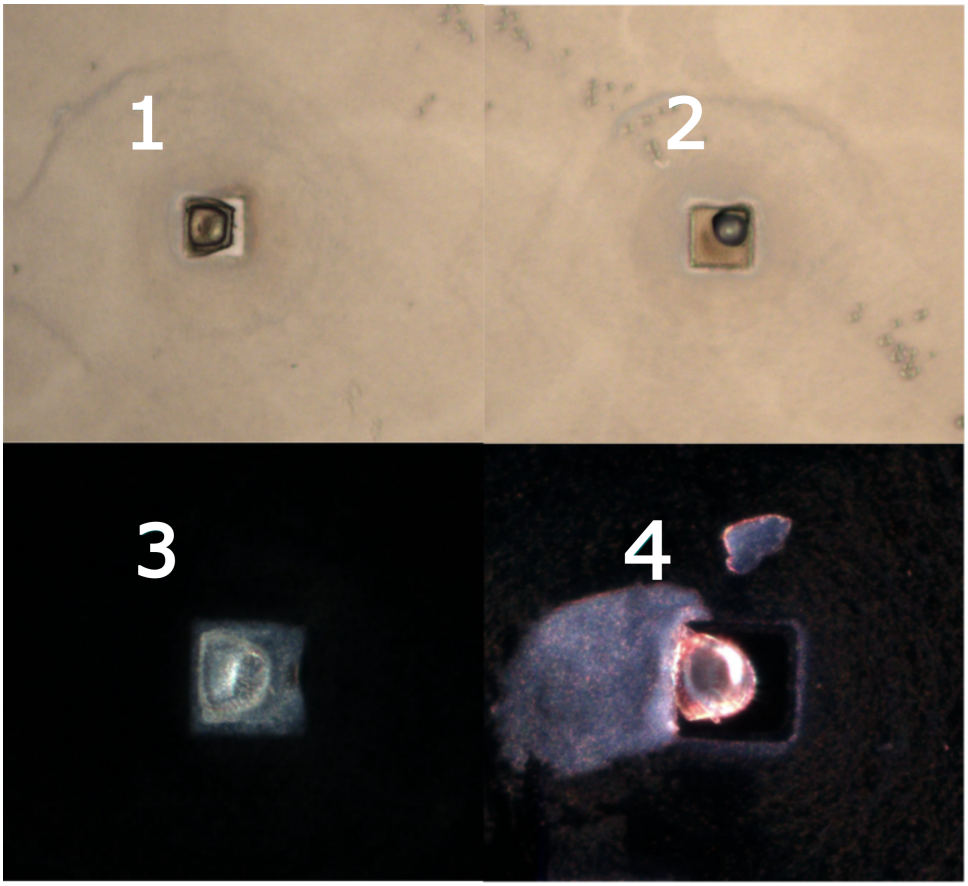


Figure 3.7: Cubes sintered with an increased laser power. Cube 1 shows that the layer can also detach from the substrate. The bright edge is the exposed clean substrate which becomes visible because the cube has shrunk. It is brighter than the surrounding area as there is residue of GP-Silica even after development. Cube 2 shows that even when the power is so high that the cube completely forms into a drop, the layer is still there. Cube 3 shows that the layer is not necessarily just lying on the substrate as in this observation the cube and the layer are in focus at the same time. Cube 4 shows that the layer can be removed, however the shape of the cube is also no longer retained.

To further differentiate between sintered and non-sintered material and possibly remove unsintered material a plasma asher (Zepto 119167 by Diener electronic) was used. A plasma asher is a device that creates oxygen radicals, which react with organic materials and remove them, as it was previously used for polishing IP-S resin prints in our experimental group [21]. Unsintered GP-Silica contains polymers, which are chemically organic materials. Sintered GP-Silica should only contain glass, which is resistant to oxygen radicals. The results of plasma ashing a partially sintered array of GP-Silica cubes (see Figure A.2 in the appendix) show that even the unsintered structures, such as the small marker in the top left, do not vanish. Nanoscribe stated that the percentage of glass particles is below 40% [12], which seems to already be too high for this application, so the unsintered parts likely become passivated against the plasma.

Another option to remove unsintered materials is using NMP (N-Methyl-2-pyrrolidon) as a solvent in an ultrasonic bath. NMP is a solvent that removes plastic efficiently. The results of this treatment showed that the adhesion of the sintered structures is a limiting factor in reference to finding a solution for removing residues of unsintered GP-Silica, as the cubes detach from the substrate before sufficient parts of the polymer are removed.

## 3.3 Coupling Depth and Finesse measurements

To verify that the structures are made out of glass and to characterize the optical properties of GP-Silica prints, the samples are placed inside the vacuum fiber microscope (see Figure 3.8). The setup features a

scannable cavity consisting of a fiber mirror and a macroscopic mirror substrate, onto which the structures of interest are printed. Through the cavity reflection signal it is possible to measure the resonances at different wavelengths and, therefore one can measure optical properties such as the Coupling Depth and Finesse.

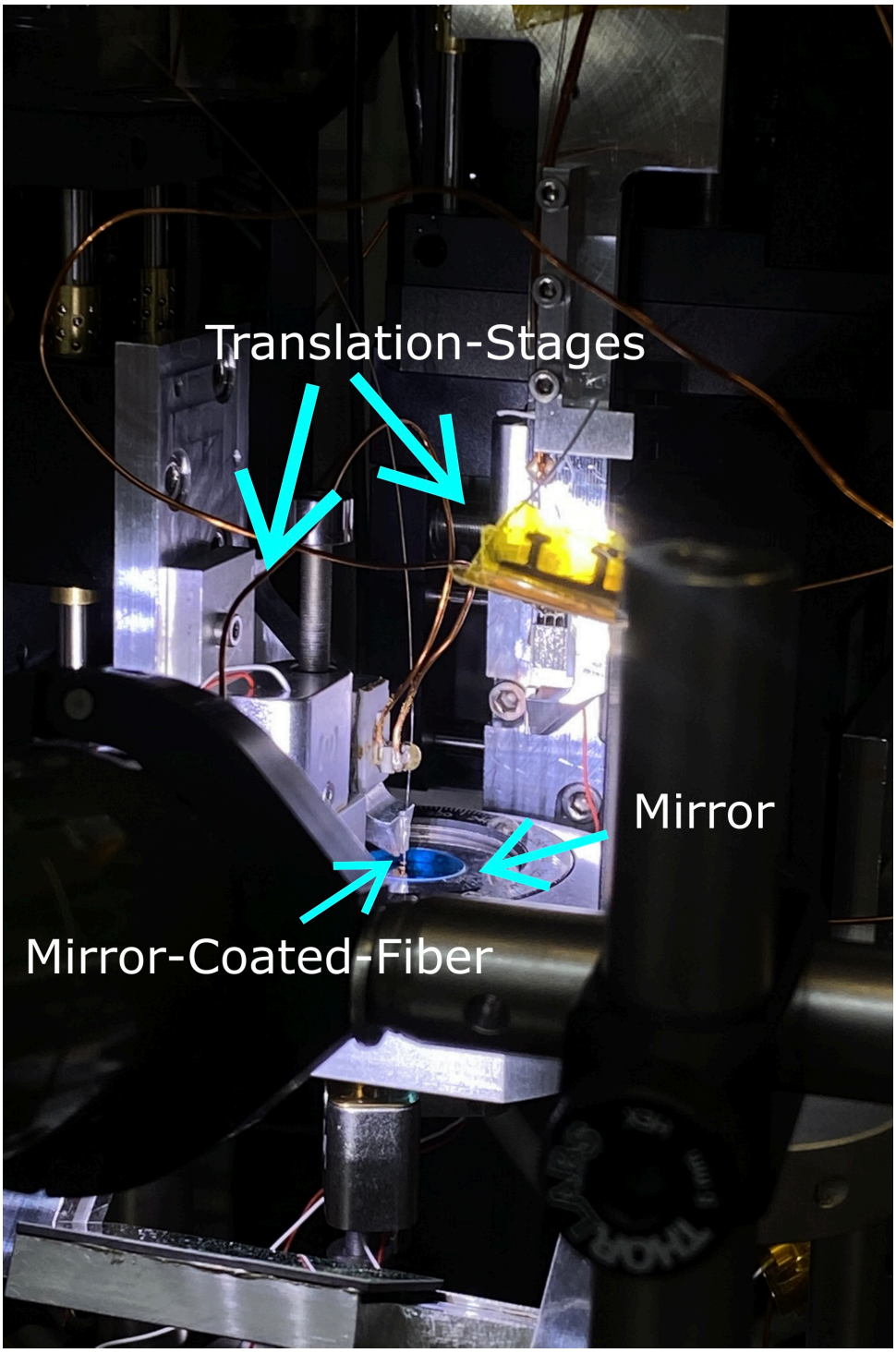


Figure 3.8: In this picture, the vacuum-fiber-microscope is shown. The mirror, on which the structures are printed, as well as the translation stages used to align the fiber mirror with the opposing mirror substrate, are visible. In this case, the measurement is not performed under vacuum conditions.

For these measurements, the cubes are printed onto a dielectric Bragg mirror. The surface of those mirrors are more reflective to the laser of the printer than the ITO-substrates. The dose therefore needs to

be adjusted. In Figure 3.9, an example of an overexposed cube is illustrated. The development of gas bubbles due to local rapid overheating of the resin is noticeable [22].

Figure 3.9: *Left*: Inside the Nanoscribe, the laser beam induces bubbles in the resin due to overheating. *Right*: Developed overexposed cube printed for the first time on a dielectric Bragg mirror. The bubbles remain visible even after development, and additional leakages have appeared.

Therefore, a new dose sweep was done, which is shown in Figure 3.10. There, one can see that if the laser power is too high, the structures leak. This is probably due to the proximity effect, which is very strong for GP-Silica resin. The proximity effect denotes the undesired polymerization of neighboring voxel lines induced at sub-threshold exposure levels [23]. These leakages already become visible inside the 3D printer, where the undeveloped structures can be observed via a camera.

Additionally, it is noticeable that underexposed structures also develop leakages. The leakages from underexposure occur during the development process. A possible explanation for this is that the voxel size decreases with lower dose, and therefore the consistant hatching and slicing distance in this array is not sufficient for the voxel lines to interconnect properly. The best reproducable dose printing parameters for cubes on the Bragg mirror are: LP = 45 %, ScSp = 5 000 $\mu$m/s[1].

[1] $SD = 0.18\,\mu m$ and $HD = 0.08\,\mu m$ (cubes/membrane-legs); $SD = 0.15\,\mu m$ and $HD = 0.05\,\mu m$ (membrane) were not changed throughout this project

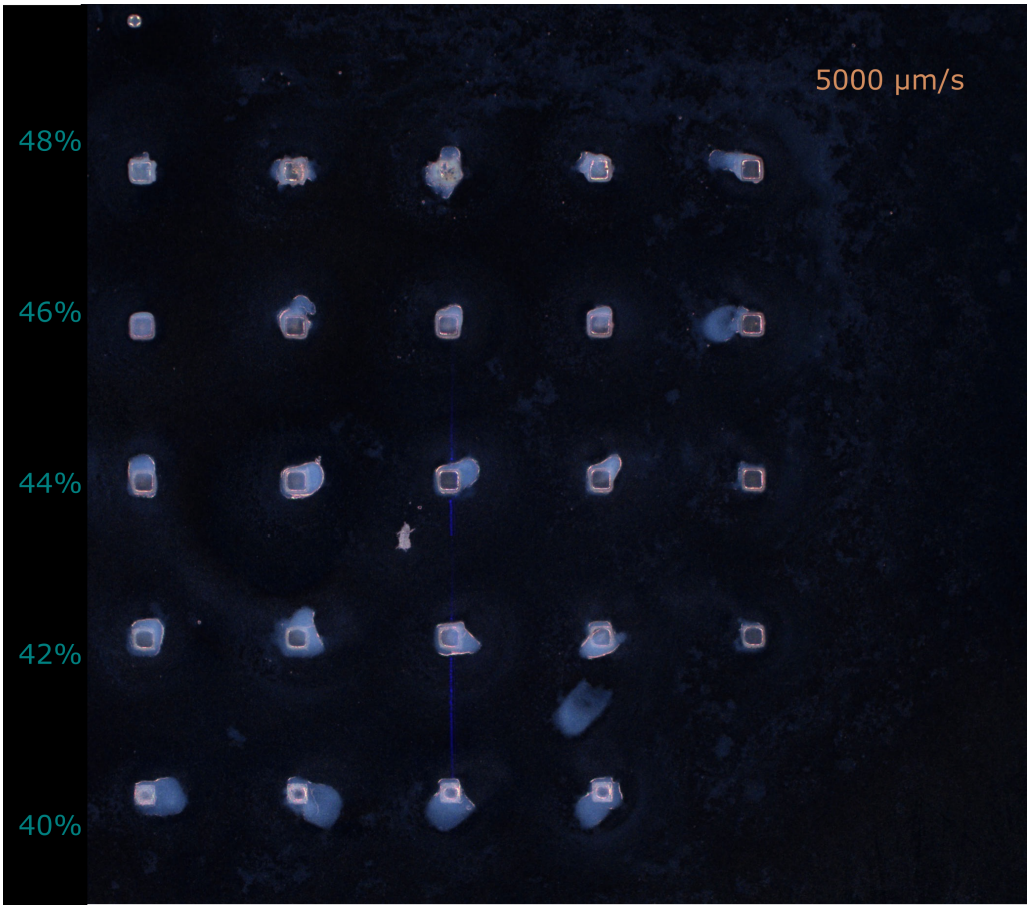


Figure 3.10: In this dose sweep on a mirror, the laser power was varied from 40-48%. It can be seen that leakages occur at every laser power. However, there are tendencies where leakages occur the least, in this case at 44%. It was also observed in the printer that bubbles no longer formed at 44%, and that at 42% and 40%, the edges of the cubes showed very low contrast, which indicates that the laser power was too low there.

The shooting parameters are the same as on the ITO substrate and the behavior of the first printed layer did not change significantly.

Once the printed and developed cubes on the mirror have been sintered, the mirror must be cleaned. As mentioned earlier, this is tricky because the adhesion of the residue is stronger than the adhesion of the main structures. After 5 minutes in an ultrasonic bath with NMP at a temperature of 45–55 °C, cubes with an expected height of approximately 8 $\mu$m vanished from the mirror. With the exact same parameters, some of the approximately 1.5 $\mu$m high cubes remained attached to the mirror, while others did not (see Figure 3.11), whereas the residues still remained.

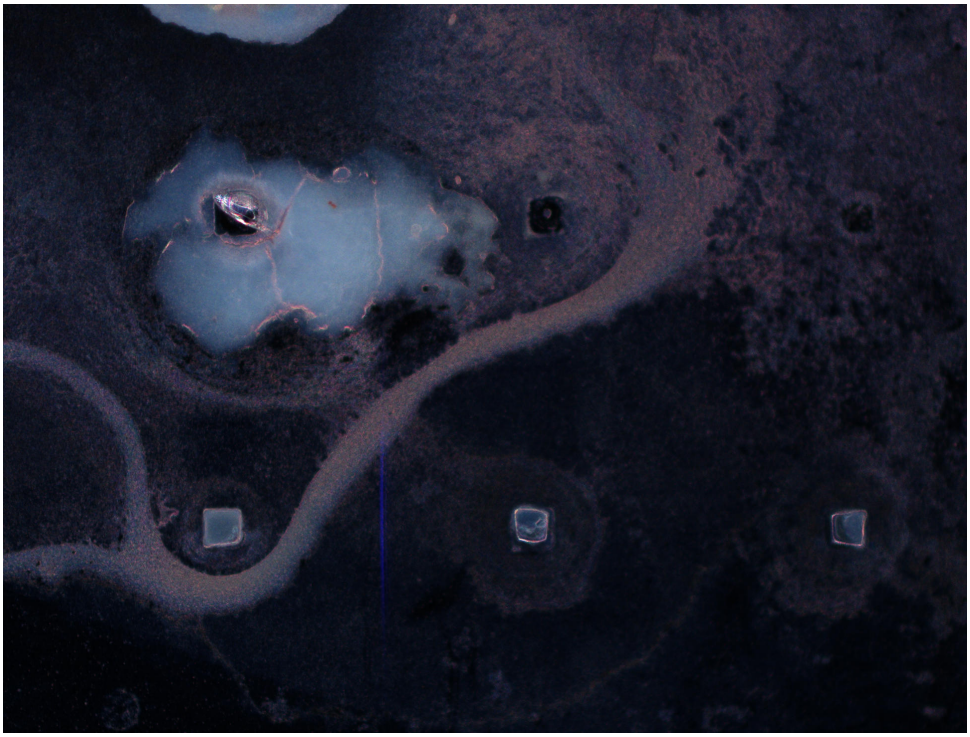

Figure 3.11: After NMP - ultrasonic bath, for 5 min with ~ 55 °C, 2 of 6 cubes have detached while the large patches of uncontrolled polymerized resin are still there.

The height could be measured with an SEM image, but at this stage of the experiment the exact height was not relevant. The dimensions given to the Nanoscribe printer do not correspond to the actual sizes after development due to proximity effects and expected shrinkage [20]. The sintering process also changes the dimensions of the structures. As mentioned earlier, this change is more homogeneous when done with the recommended method of sintering in a vacuum oven. To measure the coupling depth, the mirror was mounted into the vacuum fiber microscope (see Figure 3.8). The first measurement of the coupling depth of the glass cubes is shown in Figure 3.12 (bottom). The image at the top demonstrates that the cubes were not optimally sintered. The correct shooting parameters from the ITO substrates were not highly reproducible; however, with a larger sample size, the results should become more reliable. For printing directly on the mirrors, the printing duration should be reduced to a minimum. It was observed that residues are minimized when printing for 20 min and developing immediately afterwards. Nevertheless, streaks of GP-silica remained on the mirror surface even in this case. The very low coupling depths of at most ~8% may result from the sintered cubes not being homogeneous, from non-flat or rough surfaces, or from residual contamination. As a consequence, scattering is not minimized and the coupling depth remains very low. It can be seen that for the central and the right cube (in the figure), the regions where the surface of the cube is supposedly less uneven (as judged from bright-field microscopy) exhibit a slightly increased coupling depth. However, misalignment of the cavity can also lead to an overall reduction in coupling depth in this measurement. Although the optical quality appears generally promising, a measurement with an atomic force microscope (AFM) would be beneficial to examine the reasons for the poor coupling depth. Such measurements could potentially reveal valleys in the cubes or allow a quantitative characterization of the surface roughness. The finesse measurement typically includes 50–100 scans at several points of the structure in order to average out external fluctuations not related to low finesse, such as losses caused by mechanical noise of the piezo stack attached to the fiber. However, in this case, a finesse measurement would not yield additional insights due to the already very low coupling depth.

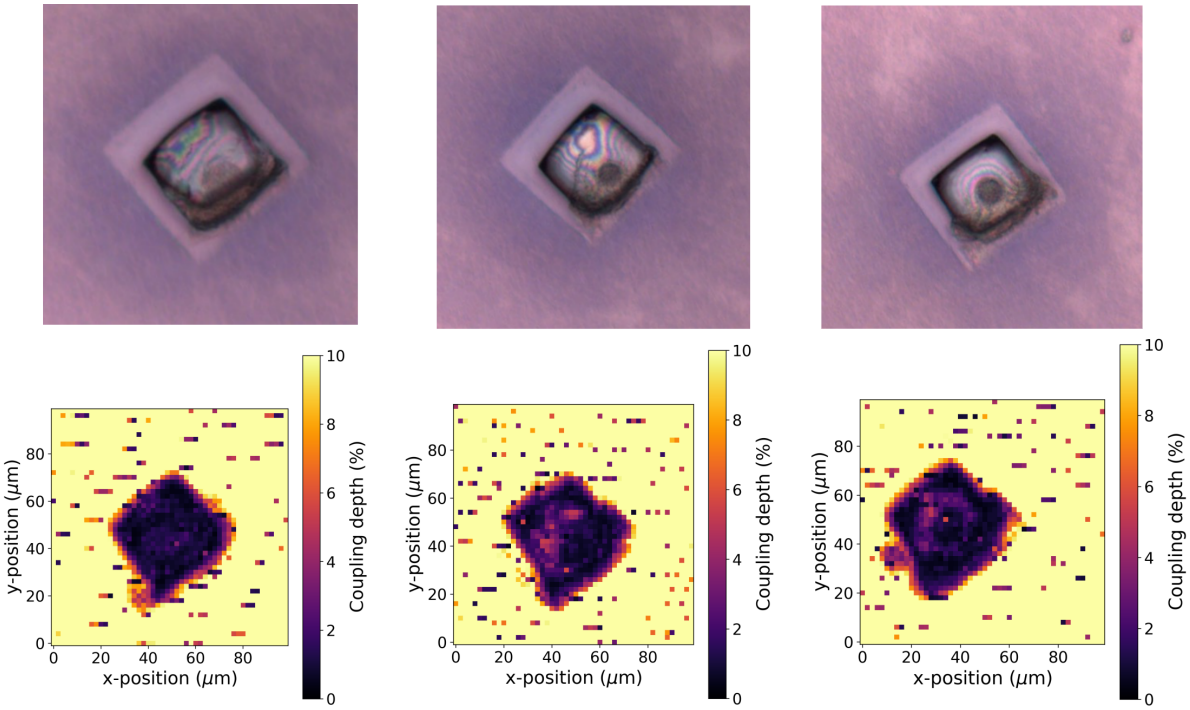


Figure 3.12: *Top*: Sintered cubes on a mirror fabricated with printing and shooting parameters similar to those used previously. It is evident that these cubes were not optimally sintered; they exhibit optical properties characteristic of fully sintered GP-silica. In bright-field microscopy, the structures appear brighter. Furthermore, the cubes have shrunk due to the sintering process, and their surfaces tend to be non-planar, partly because of the shooting defects visible in the second and third cubes. *Bottom*: Coupling depth measurements performed with the VFM. The $x$-axis and $y$-axis represent the dimensions of the scanned area of 100 µm × 100 µm, and the color code indicates the coupling depth in percent, where the maximum value is limited to 10% for better visualization. The areas surrounding the cubes exhibit coupling depths of approximately 40% ∼ 50%.

CHAPTER 4

# Development and characterization of GP-Silica sintered membranes

In this chapter, the fabrication of GP-silica membranes produced by two-photon direct laser writing and subsequently sintered using a $CO_2$ laser is optimized. First, the reproduction of membranes from the previous work is carried out in Section 4.1. This is followed by the exploration of different geometries (see Section 4.2). Finally, in Section 4.3 a new approach is introduced in which IP-S-printed scaffolds are used to stabilize the GP-silica printed membranes.

## 4.1 Reproduction of the previous membranes

As a first step, the results from the previous work were reproduced. For this purpose, membranes with the exact same geometry and printing parameters as those yielding the best results in the previous work were fabricated, namely:

- Membrane dimensions: $100 \times 100\,\mu m$, thickness: $2\,\mu m$
- Printing parameters for the membrane:
  - Slicing distance: $0.15\,\mu m$
  - Hatching distance: $0.05\,\mu m$
- Printing parameters for the feet:
  - Slicing distance: $0.18\,\mu m$
  - Hatching distance: $0.08\,\mu m$
- Laser power (LP): 85%
- Scan speed: $7500\,\mu m\,s^{-1}$

Using a fresh batch of GP-Silica resin, the previous results were succesfully reproduced. Figure 4.1 shows the best results, closely resembling the results from the previous work, shown Chapter 2 in Figure 2.4(a).

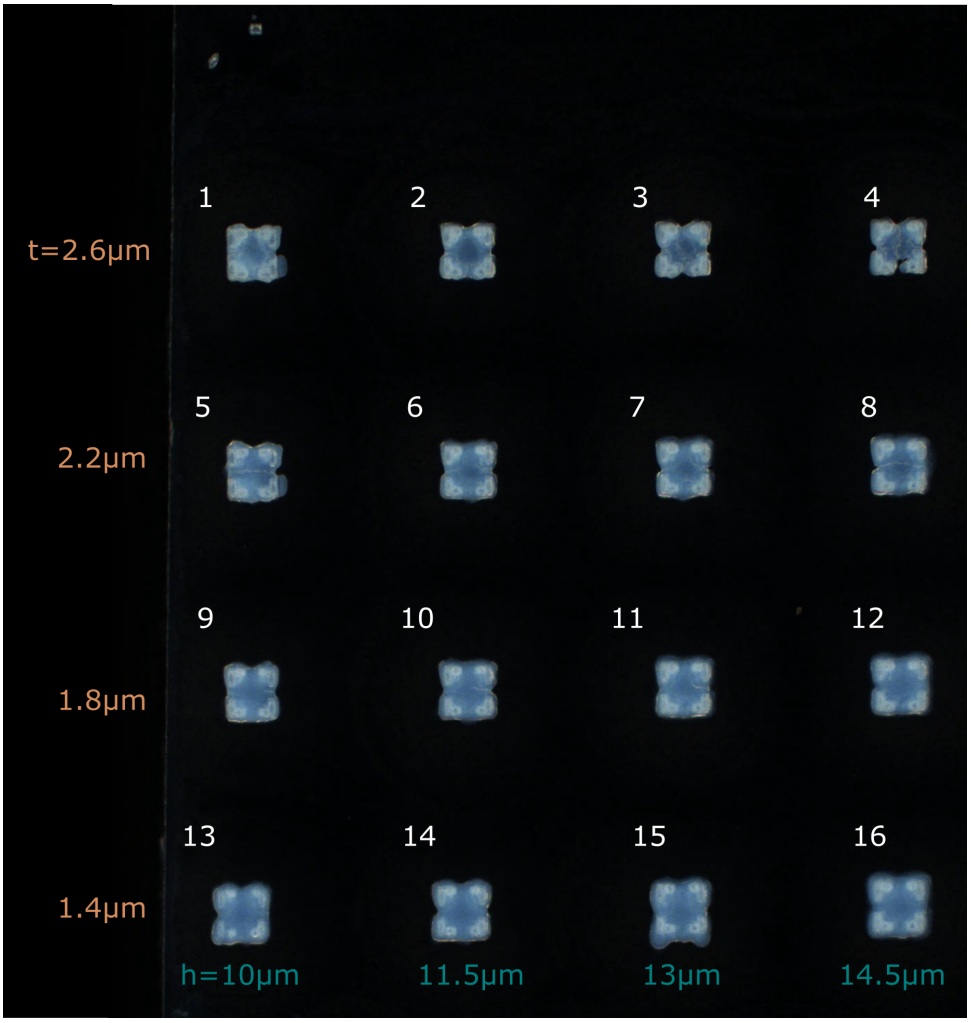


Figure 4.1: Illustrated is the variation of the foot height ($h$) and the membrane thickness ($t$), with LP = 60% and ScSp = 8500 $\mu$m/s. With increasing height, the stability tends to decrease, which is most evident for the thickest membrane 4. In contrast, the thinnest membranes 13-16 exhibit slightly blurred edges. Overall, the membranes appear comparable to the previous results: no major leakages, relatively well-defined edges, and no pronounced cracks are observed.

Using the light microscope, the samples can be observed in two different modes: bright-field and dark-field. Each mode offers distinct advantages and disadvantages. In dark-field mode, even very faint residues and features that are less recognizable in bright-field mode can be detected. In bright-field mode, finer differentiation between focal planes is possible. For example, when focusing on the outer layer of the membrane, it appears free of cracks. However, focusing slightly deeper reveals that the structure is uneven and of generally poor quality. In contrast, such defects are less pronounced in dark-field mode.

Further investigation of these membranes using especially the bright-field mode, revealed that the membranes had considerable defects upon closer examination. In Figure 4.2, one can see that the use of dark-field mode to judge the structure quality, which was mainly used in the previous work to judge the success of fabrication, is not sufficient. In general, the characterization is limited, when using the light microscope, as it is only possible to observe very obvious malfunctions such as large cracks, leakages, or bubbles. While the height is not verifiable in an absolute sense, as mentioned earlier, the height and features of the membranes can be roughly estimated by viewing them in different focus planes.

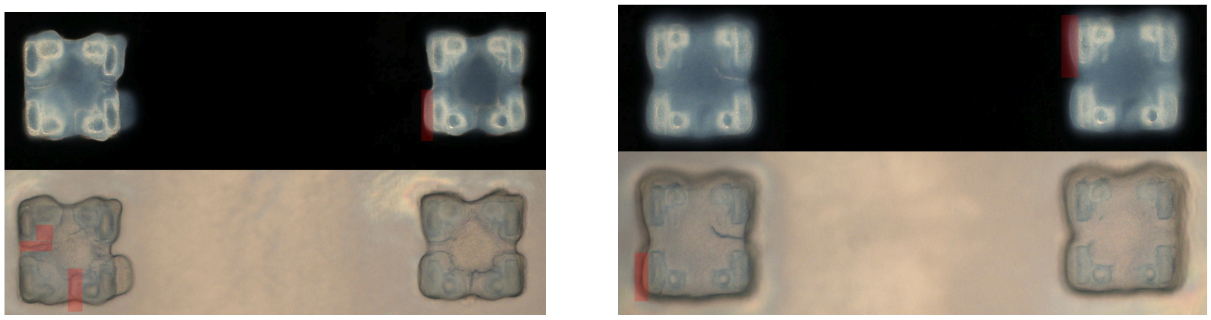

(a) (b)

Figure 4.2: (a) Dark-field and bright-field comparison of membranes with a thickness of 2.6 µm; *left*: height 10 µm, *right*: height 11.5 µm. It can be observed that when the focus is set to the plane of the feet, the quality appears significantly better in dark-field mode than in bright-field mode. In dark-field mode, the defects appear minimal, whereas in bright-field mode it becomes evident that the membranes are likely not sufficiently free-standing. They appear either to have sagged or for the feet to have expanded (see red highlights) in such a way that the membranes are presumably only minimally free-hanging.
(b) Dark-field and bright-field comparison of membranes with a thickness of 1.8 µm; *left*: height 13 µm, *right*: height 14.5 µm. It can be seen that the edges (see red highlights), which in dark-field mode appear only slightly expanded, appear significantly more pronounced in bright-field mode.

In Figure 4.2, one can see that the edges of the feet are sharp, but there is another organic-shaped layer (red-marked in 4.2) around them. It is very likely that the membrane also has this layer, possibly on both sides. This observation led to the question of whether the membranes are even suspended above the substrate with an appropiate spacing between the substrate.

Another observation was that in bright-field it was potentially possible to see through the membrane. This is noticeable in Figure 4.3, when focusing on the uppermost layer, it seems that the membrane is intact, but when the focus shifts to a lower-lying layer, it appears as though the membrane is broken or has collapsed in on itself. There are two possible explanations for these observations. It could be that the membrane itself closes the gap because of expanded edges which surround the in principle sharply printed edges, or is not stable enough and sinks to the ground. Another explanation could be that unpolymerized resin becomes trapped under the membrane, leading to a flushing problem during the development process.

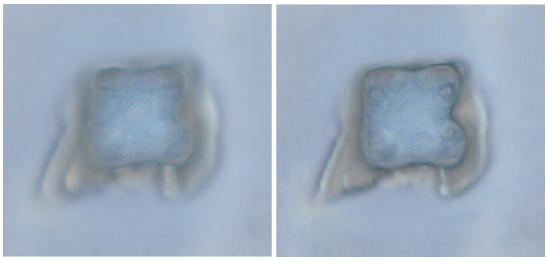

Figure 4.3: *left*: Uppermost layer is in-focus, the membrane looks even. *right*: Lower layer of the membrane is in-focus, defects get more visible.

In conclusion, the membranes looked acceptable in darkfield mode from a top-down perspective, but when analyzing them with different light modes and focus depths, and considering the problematic layers surrounding the sharply printed feet, there is a very high probability that the membranes are not free-hanging structures in this state.

## 4.2 Further development of the membranes

To verify this hypothesis, the membranes got printed on the edge of the ITO substrates. The setup is shown in Figure 4.6, because this allows viewing the structures from a 90° angle even with the previously used light microscope. The substrate is taped onto a holder and then placed inside the Nikon ECLIPSE LV100ND microscope (see Figure4.5). The schematic which illustrates the 90° perspective of the membranes is shown in Figure 4.7.

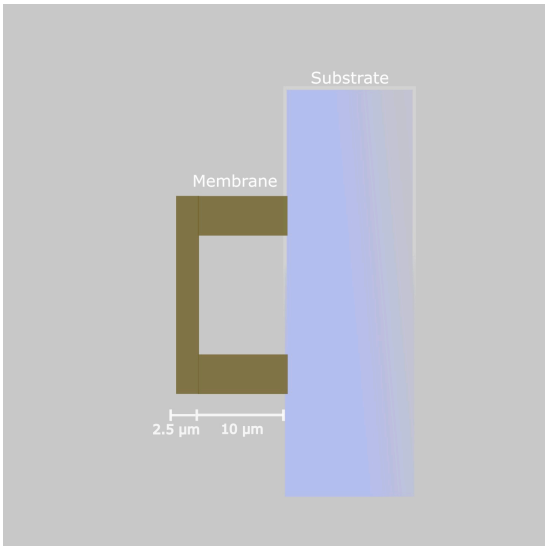


Figure 4.4: Schematic of the 90° angle view of the membranes printed onto the edge of the ITO substrates.

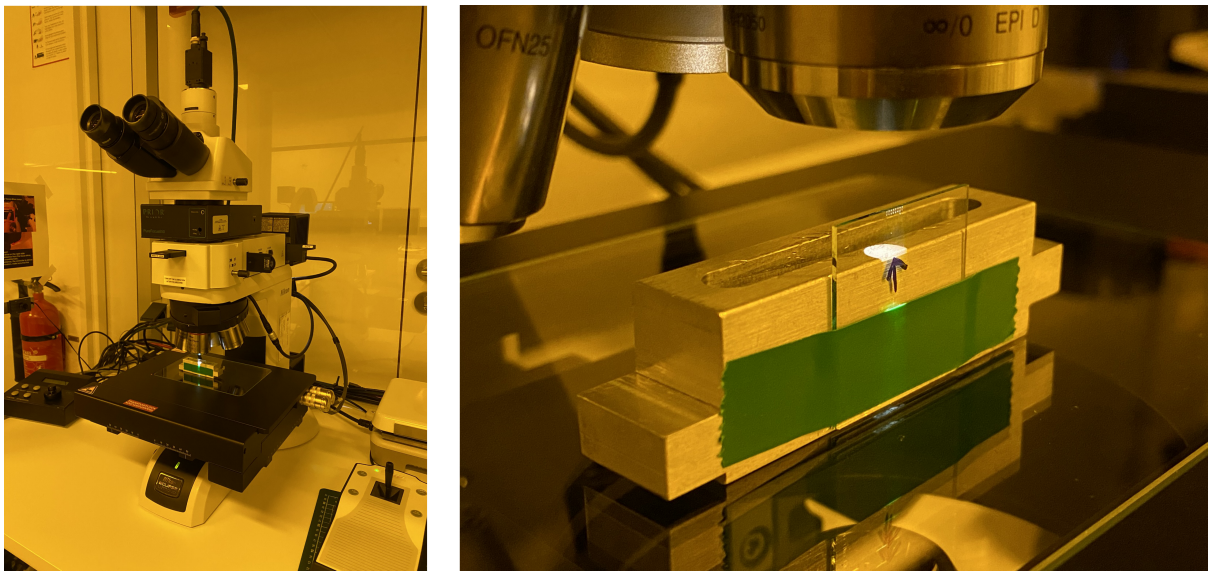

Figure 4.5: In the image, the Nikon ECLIPSE LV100ND microscope is shown, which was mainly used, to observe the membranes from a 90-degree perspective. The substrate, on which the membranes are printed, gets taped onto a holder and placed inside the microscope as shown.

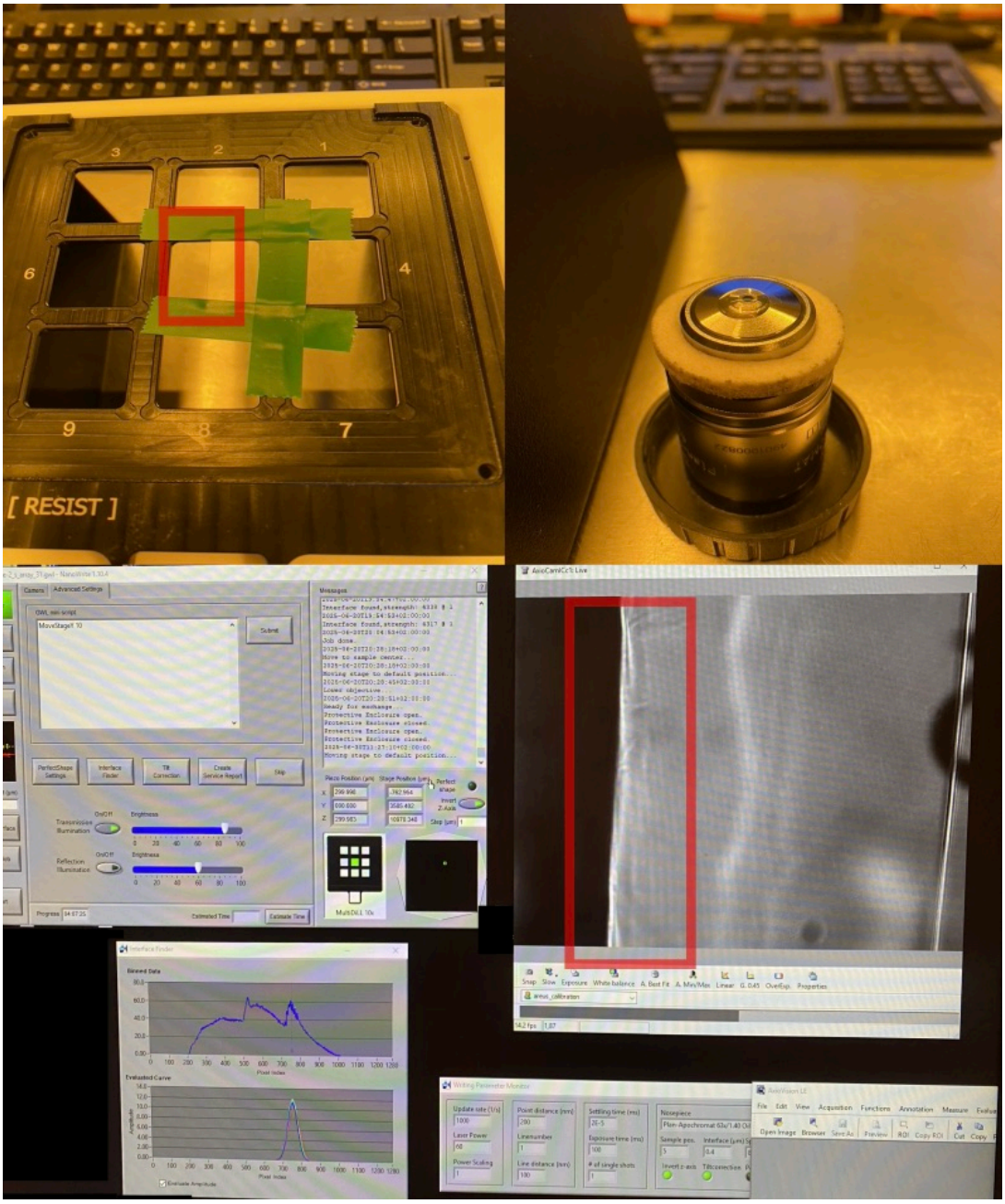


Figure 4.6: At the top of the image, the procedure for "on-substrate-edge" prints is illustrated. The ITO substrate, which is normally cut to fit the holder with its center aligned to the optical axis, was instead positioned with its edge at the center and fixed in place with tape (*left*). The resin is applied to the objective rather than directly onto the substrate edge (*right*) to ensure that the resin does not need to be applied to the edge itself. At the bottom, the NanoScribe software *NanoWrite* is shown. Highlighted is the internal view from the printer during an on-edge print, where the edge is clearly noticeable, facilitating alignment and enabling structures to be printed very close to the edge.

In Figure 4.7, one can see that the proposed hypothesis is indeed correct. Only very few membranes showed small gaps between the membrane and the substrate. The other ones, which also looked fine from a top-down perspective, did not show any gaps.

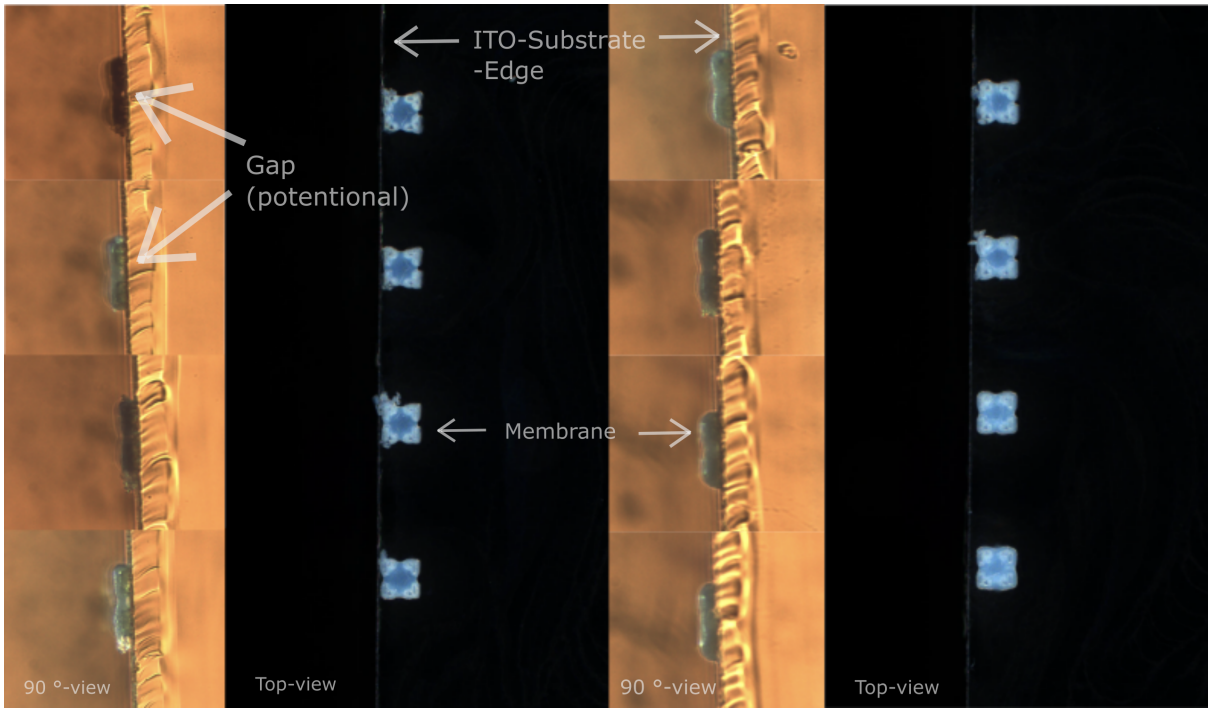


Figure 4.7: In this picture, the membranes are shown for the first time from a 90° angle using the light microscope (see Appendix A.3). The same membranes are shown from a top-down perspective, positioned directly next to each 90° view, in dark-field mode. It can be observed that, although the membranes appear intact from the top-down perspective, only two out of the eight membranes exhibit a possible small gap.

The first approach to solve this issue is to try different geometries to achieve better flushing. Because GP-Silica printing is very sensitive to the laser dose, any significant change in geometry requires determining a new correct laser power, which lies within a very narrow parameter range.

The legs of the previous membranes had an L-shape. The CAD model is illustrated in Figure 4.8(a). The legs create sharp, narrow spaces where flushing the resin away could be difficult. For this reason, an approach with triangular legs was taken (see Figure 4.8(b)).

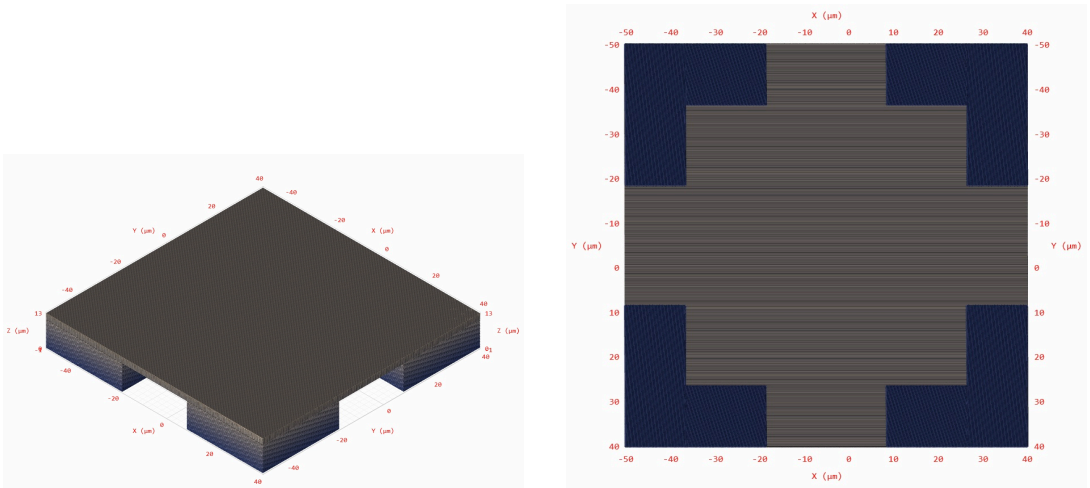

(a)

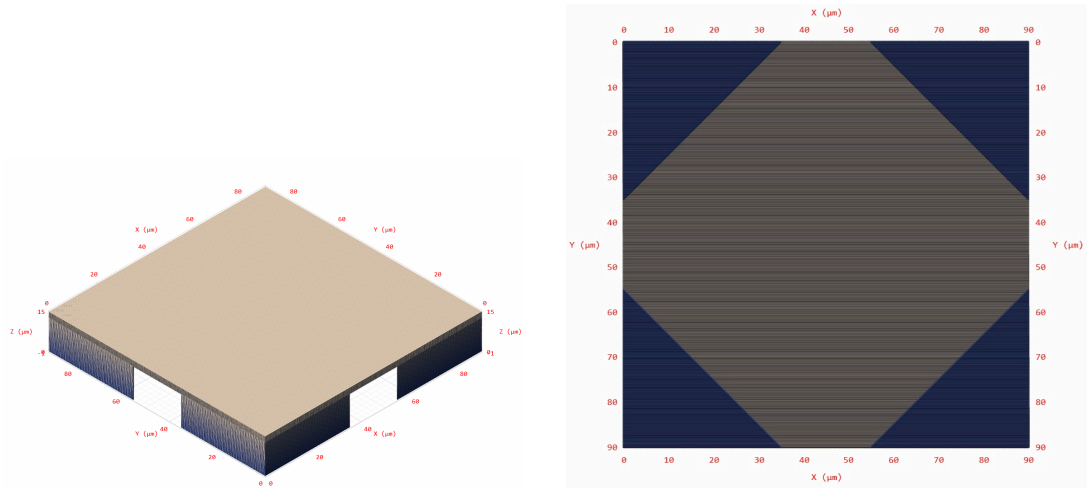

(b)

Figure 4.8: CAD overviews of membrane geometries. (a) Shown is the CAD model, created in *Describe*, of the previous membrane geometry (*left*) and the underside view, where the L-shaped feet are shown (*right*). (b) Shown is the CAD model, created in *Describe*, of an alternative geometry with triangular-shaped feet (see *right*) designed for improved flushing.

The results of this geometry showed that the laser power/dose was incorrect when using the same parameter ranges as for the previous membranes (see Figure 4.9). Since further investigation of these poor results would have been very time-consuming, other geometries were explored. A simpler approach was a table-like configuration. This geometry turned out to be not very stable, the results and the CAD model are shown in Figure 4.10. The leakages indicate that the dose was not correct for this geometry either, and that this geometry also does not lead to better overall results.

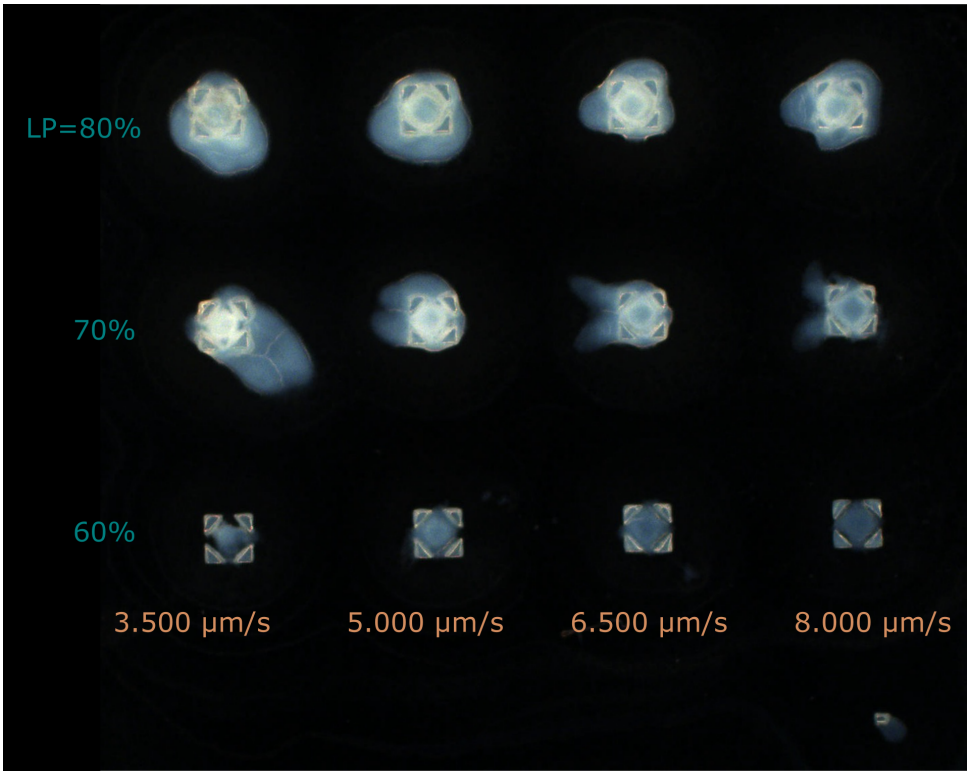


Figure 4.9: A dose sweep was performed, the image shows that the membranes exhibit very severe leakages. However, even the marker leaks, indicating that this issue may not necessarily be due to the new geometry. It can also be observed that, with reduced laser power (60%), the membranes are not stable either.

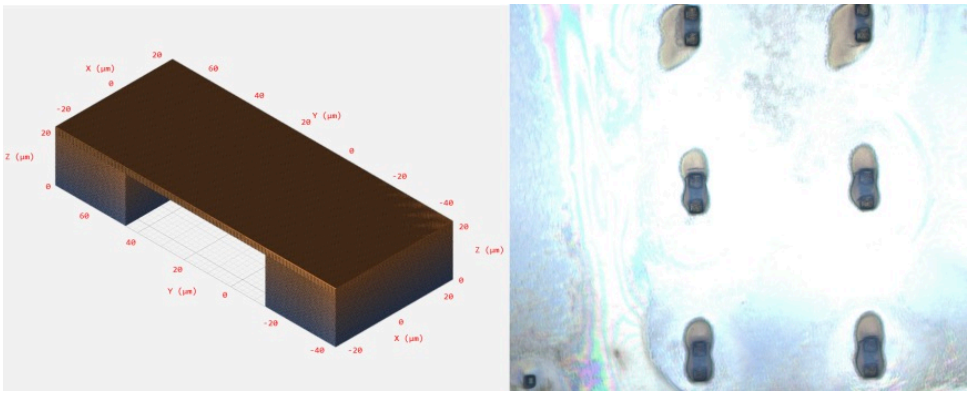

Figure 4.10: In this image, the CAD model of the simple table geometry, created in *Describe* (*left*), is shown alongside the results exhibiting large leakages and no well-defined edges (*right*).

Therefore, the original square-shaped geometry with the L-shaped legs needed to be optimized. To address the flushing issue, the height was increased. Ultimately, the micro-fiber cavities are not restricted in length at this stage of the experiment. The increased height could solve the missing gap, regardless of whether it is caused by flushing problems or by expansion and sagging of the membrane itself. When the membrane with the old geometry is increased in height, the structures require improved adhesion, otherwise they do not adhere properly to the substrate. This effect was observed and may be attributed to the increased mass. For this reason, support areas were implemented (see Figure 4.11) to increase the contact area with the substrate. The support areas worked and the structures adhered to the substrate. The results are shown in Figure 4.12.

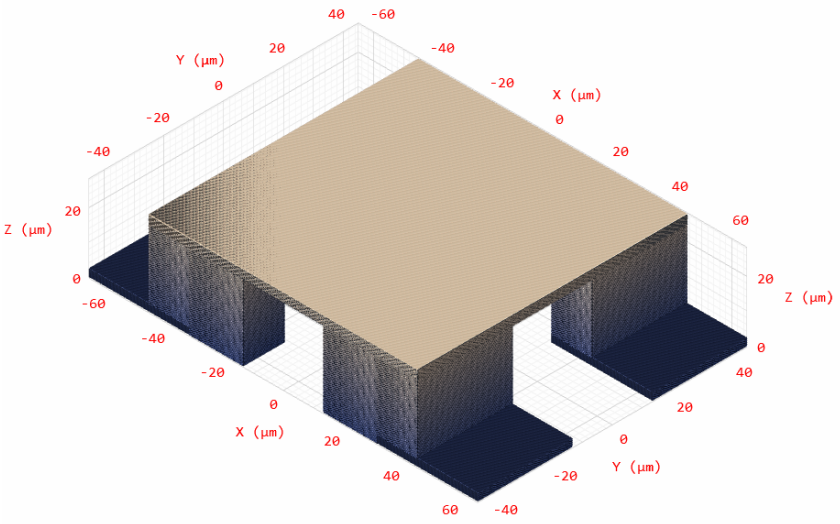


Figure 4.11: Shown is the CAD model, created in *Describe*, of the initial membrane geometry (with L-shaped feet) but with the height increased from 10 $\mu$m to 25 $\mu$m, and with additional support areas underneath the feet to increase the contact area between the substrate and the structures, thereby improving adhesion.

However, it can be seen that leakages increased again. Since the correct dose has not yet been determined for these new additions. The leakages appear near the substrate, where the new additions are located and not in the upper layers of the structures. A possible consideration is that the substrate reflects a small percentage of the laser light. This reflected light could potentially interfere with the primary laser light and polymerize the resin in an uncontrolled way. The leakages are not critical in this case, because the relevant parts of the structures are mainly the membrane and the legs. It is also observable that some of the membranes were not stable. This is due to a thickness sweep, the higher the feet get printed the less stable the thicker membranes get.

Viewed from a 90° angle, as seen in Figure 4.12, the 25 $\mu$m high membranes, in comparison to the 10 $\mu$m high membranes, are not 2.5 times higher. The very rounded edges lead to the interpretation that the membranes sank into themselves, rather than the flushing being the main issue.

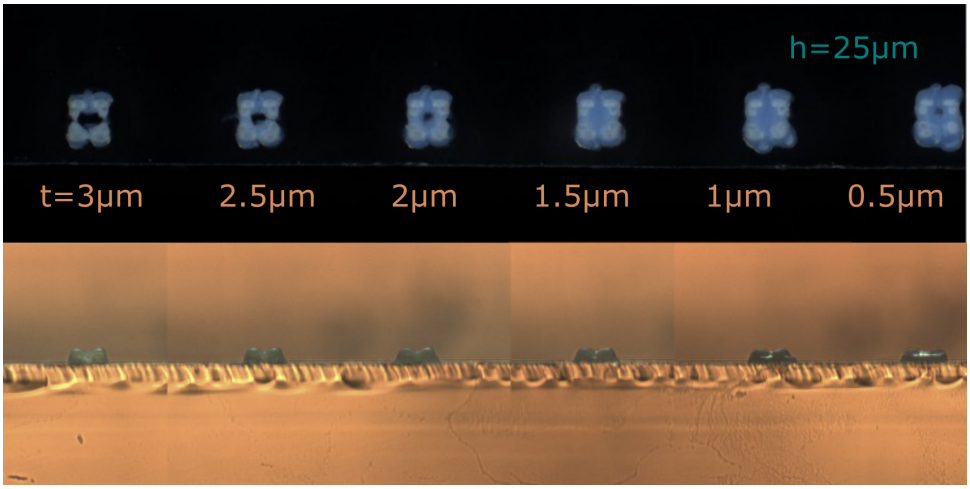


Figure 4.12: In this image, the results of the increased-height membranes are depicted. As previously observed, when the membrane height exceeds 10 $\mu$m, thicker membranes tend to collapse. At a height of 25 $\mu$m, a thickness of only 2 $\mu$m already leads to instability. Viewed from a 90° angle, even the membrane with a thickness of 1 $\mu$m,which appears satisfactory from the top-down perspective, does not exhibit a visible gap.

## 4.3 IP-S-scaffold approach

To ensure that the membranes are free-hanging, another approach to print GP-Silica membranes with dimensions $\leq 100 \times 100\,\mu$m needs to be taken. The idea of the new approach is to force a gap by first printing an IP-S membrane and, on top of this membrane, a GP-Silica membrane.

IP-S is a standard commerical resin by Nanoscribe, which is structurally much more stable and not as sensitive to small changes in laser dose compared to GP-Silica. The resolution of IP-S is much larger at these dimensions compared to that of GP-Silica, which ensures that the printed geometry resembles the design geometry much more closely. The IP-S membrane ensures the stability of the structure and, therefore, the existence of the gap. Due to the increased stability of this approach, a simpler geometry is chosen, so that flushing can be done more effectively. The geometry of the printed structures is shown in Figure 4.13.

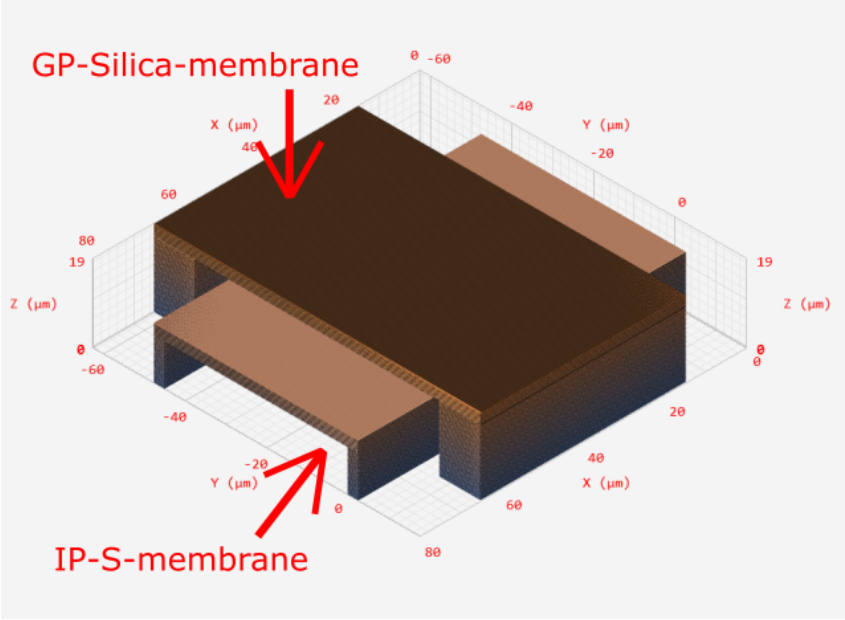


Figure 4.13: In this image, the CAD model created in *Describe* of the combined membrane print is shown to visualize the new approach. In the actual printing process, the membranes are not contained in a single CAD file, as they are printed in individual print jobs using different resins. The IP-S membrane is significantly broader, ensuring that the GP-Silica membrane does not enclose the IP-S membrane.

The size of the IP-S-printed membrane along the x-axis (see Figure 4.13) is chosen to be much larger than that of the GP-Silica membrane. This is a precaution to prevent the leaking GP-Silica from enclosing the IP-S membrane. The enclosure of the IP-S membrane must be avoided, as it needs to be removed at the end of the process. Otherwise, the $Q$-factor of the membrane would be limited by the $Q$-factor of the IP-S membrane.

The thickness of the IP-S membrane is 2.5 $\mu$m. This ensures that the membranes do not have a large volume and that there is sufficient adhesion to the substrate. The small volume is important because less material needs to be removed later.

The process of fabricating these structures is as follows: first, the IP-S membranes are printed and developed. Then, the printed IP-S membrane array is inserted again into the Nanoscribe, this time using GP-Silica resin. The coordinates need to be aligned. A sufficient and time-efficient approach to ensure proper alignment between the two prints was to mark the position of the print laser spot with adhesive tape to the computer screen. This is shown in Figure 4.14.

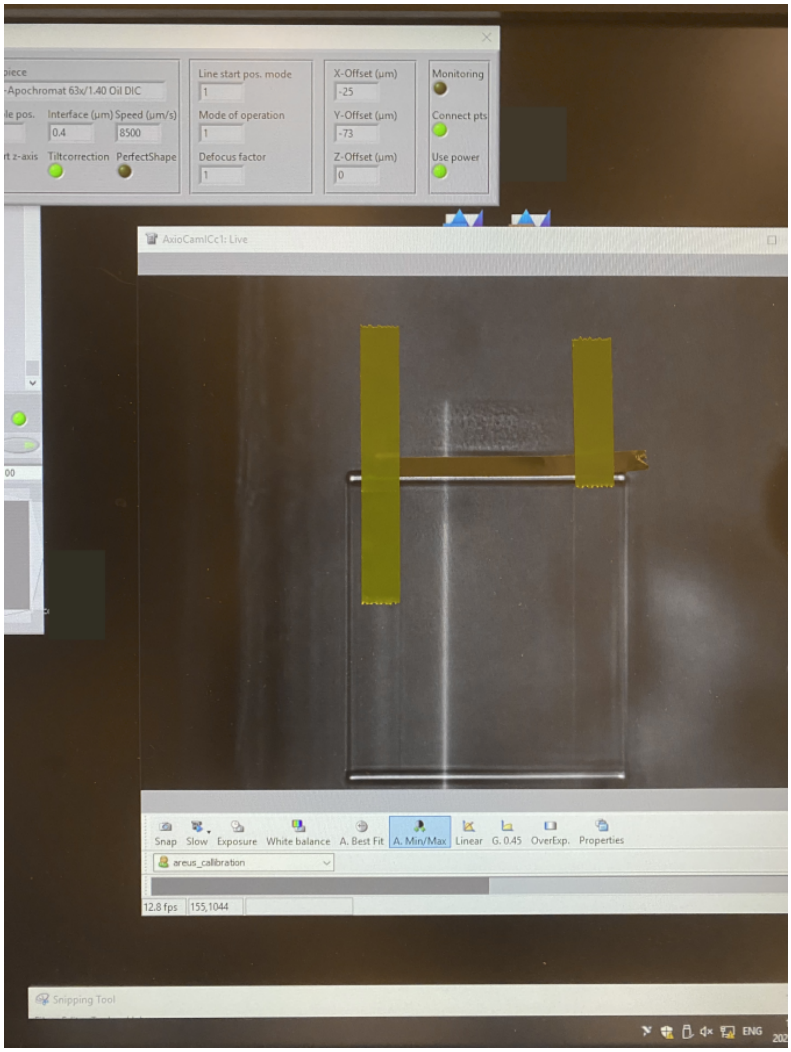


Figure 4.14: In the image, the taped computer screen is shown. The software displays the live feed from the camera inside the Nanoscribe printer. On the left side of the camera window, the edge of the ITO substrate is visible. The IP-S membrane appears as the structure with the high-contrast bar. The GP-Silica leg has already been printed in this image; it appears as the grainier layer surrounded by adhesive tape. The edges of the GP-Silica membrane on top of the IP-S membrane are also observable.

For alignment, it is easier to make the GP-Silica membrane slightly longer along the $y$-axis than the extent of the IP-S membrane. However, in that case, the GP-Silica membrane needs to support itself in those free-hanging areas, which can reduce stability. This is shown in Figure 4.15.

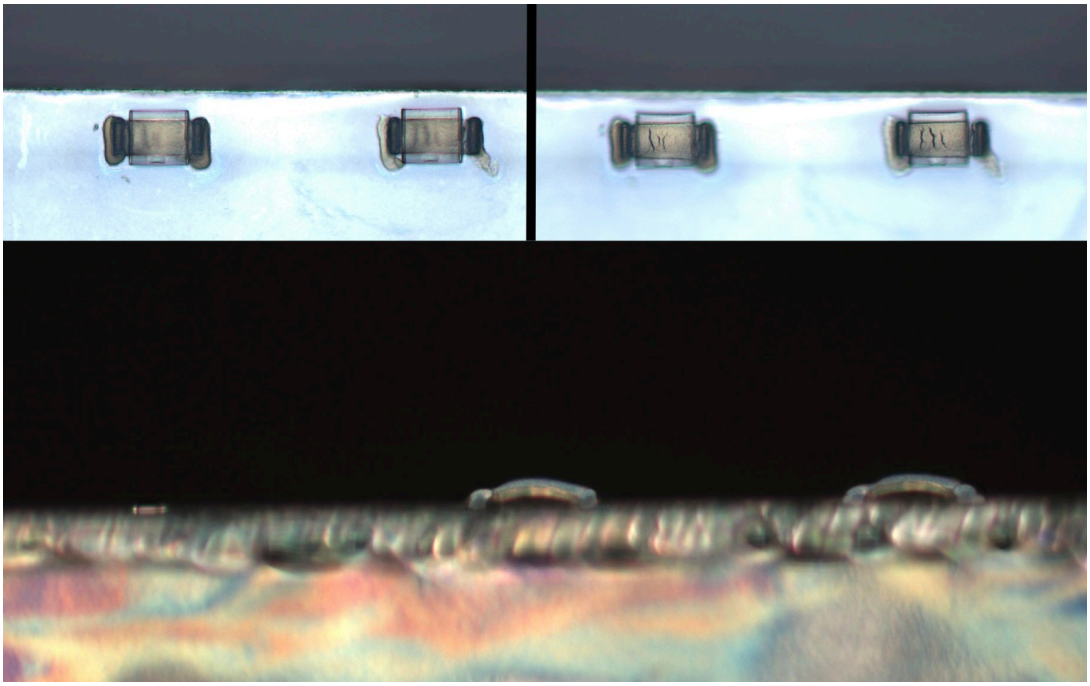

Figure 4.15: In this image, the first print of the combined membranes is shown. *Top-left*: Focus on the IP-S membrane. It is noticeable that the feet of the GP-Silica membrane are also sharp at the same time. Some leakages around the feet are visible, probably due to slight overexposure. The contact areas where the GP-Silica membrane is not supported by the IP-S membrane, but should be stabilized by its own feet, become unstable and crack. This is observable in the right membrane at the right foot. *Top-right*: Focus on the GP-Silica membrane. Here, the membranes are cracked, but the edges are well-defined. *Bottom-center*: The combined bridges are displayed from a 90° angle. One can see that the GP-Silica feet have sunk into themselves, causing the membranes to bend.

Another observation was made while printing the first combined membranes (see Figure 4.15): The GP-Silica feet which are the less defined, less transparent outer layers, did not uphold their height according to the printing parameters. In this array, the IP-S membranes were designed to have a height of 10 $\mu$m and a thickness of 2.5 $\mu$m. And the GP-Silica membrane were designed to have a height of 13 $\mu$m, with a thickness of 2.5 $\mu$m. But it is noticeable that, while the GP-Silica feet subside to a much lower height, the GP-Silica membrane was supported by the IP-S membrane. This strained the connecting parts of the membrane and the legs, which led to cracks.

To solve this issue, the subsidence of the GP-Silica prints needs to be considered when choosing the geometry of the combined membranes. By estimating the incursion through rough estimations using Inkscape (see Figure 4.16), the fitting height is approximately 18 $\mu$m, so that the feet and the membrane have the same height. The results are shown in Figure 4.17. The cracks at the connecting points decrease, and the membranes are roughly planar.

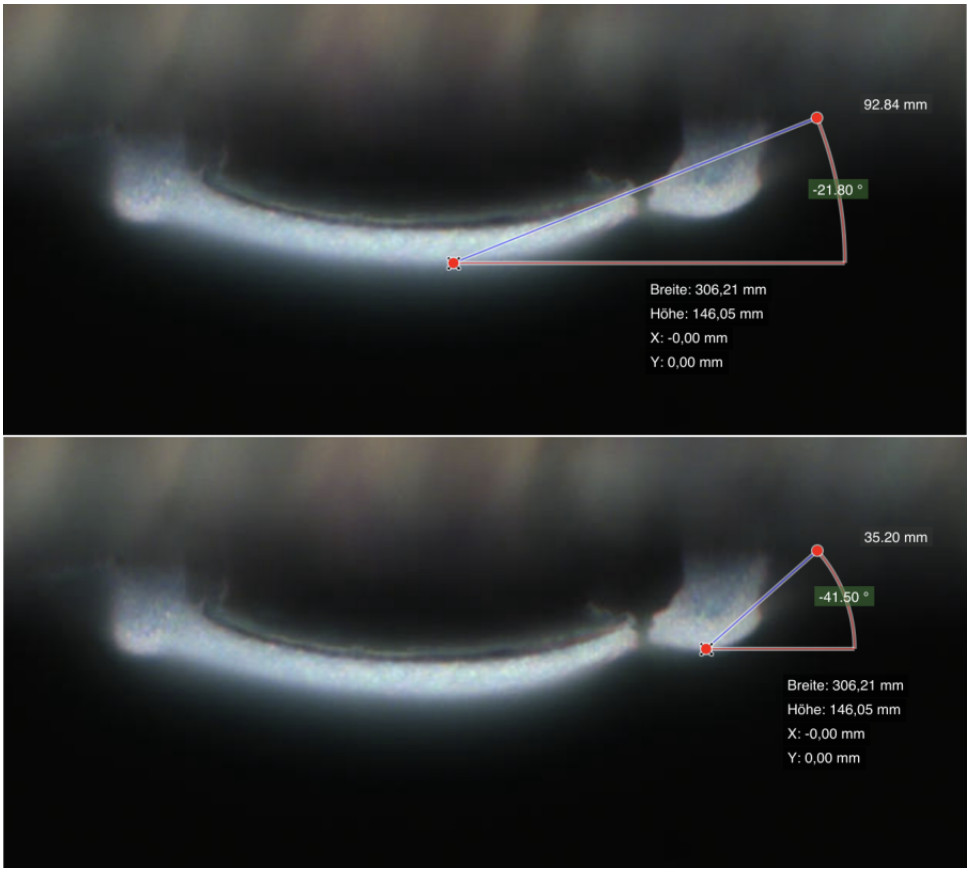


Figure 4.16: In this picture, the estimation of the subsidence of the GP-Silica feet is illustrated. The measured height difference is approximately $\frac{35}{93} \approx 0.376$, i.e., about 38%. The design specified a height of 13 $\mu$m, so 38% of 13 $\mu$m corresponds to approximately 5 $\mu$m. Therefore, if the membrane feet are designed to be about 18 $\mu$m high, they should subside to a final height of 13 $\mu$m.

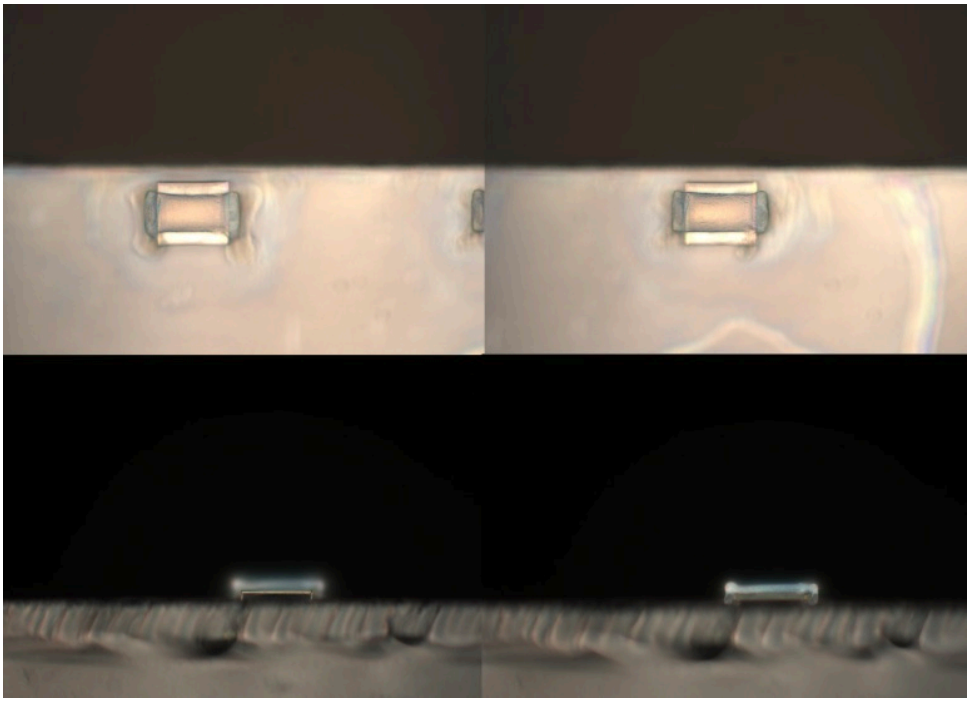

Figure 4.17: *Left*: Focus on the IP-S membrane. When the focus is set to the IP-S membrane, the GP-Silica membrane and its feet are out of focus, which is slightly visible in the top-down perspective. At the bottom, the IP-S membrane is shown from a 90° angle, where it can be seen that the membrane is now planar. *Right*: Focus on the GP-Silica membrane. With the increased height, the membrane is now free of cracks. This is observable in the top image with the top-down perspective, likely due to reduced stress because the membrane is now planar rather than bent. At the bottom, it is visible that the GP-Silica membrane is planar as well. The feet exhibit a contrast gradient, where the contrast decreases the closer the respective layer is to the substrate. This could be due to partial blocking of the laser when printing the feet directly adjacent to those of the IP-S membrane.

There are still some leakages, and the GP-Silica layers do not have sharp edges. The feet are also less defined in comparison to the not combined membranes, this can be caused by the fact that the laser beam gets partially blocked or scattered from the preexisting polymerised IP-S-Membrane during the printing process of the GP-Silica membrane. But the relevant layers, the ones forming the membrane, are homogeneous enough for this fabrication phase.

The next step of the fabrication is the sintering of these membranes. At this point, the question arises whether the IP-S should be removed in advance, afterward, or if it is even possible to remove the IP-S through the sintering process. IP-S is made out of polymers and can therefore be removed using a plasma asher (see Section 3.2.1).

In Figure 4.18, the combined membranes with a heigth of 13 µm[1] were plasma ashed with 100% power, for 2 hours. After this treatment, the IP-S layer notibly decreased visibly in volume and even detached from the substrate in some areas, but residues remained. The bulging of the membranes further increased. Bulging of the GP-silica membrane may originate additionally from stress due to shrinkage of the underlying IP-S layer during plasma ashing. Increasing the GP-silica thickness could suppress this effect by improving its weight and mechanical resilience.

[1] Although 18 µm is the optimal height, however due to lack of time, the prints with a height 13 µm were used to investigate the effects of plasma ashing as well.

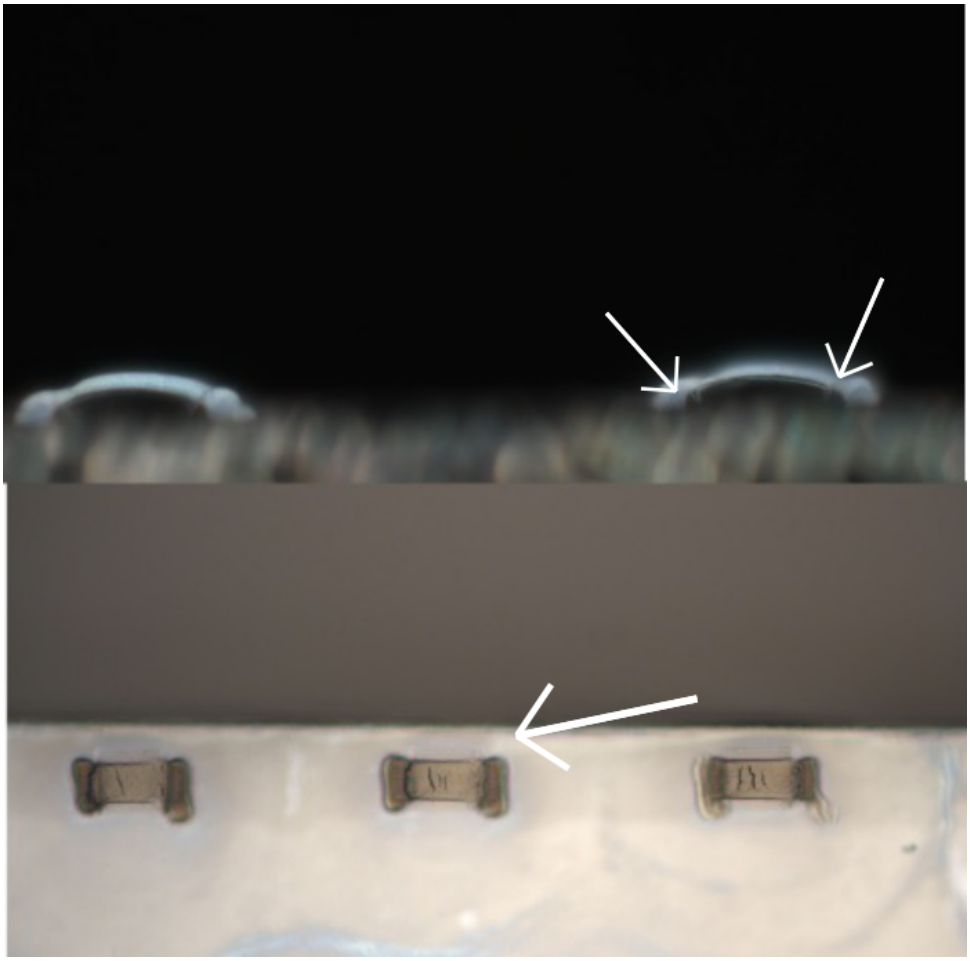

Figure 4.18: In this image, the results from plasma ashing at 100% power for a duration of two hours are shown. The top image presents a 90° angle view, and the bottom image shows a top-down perspective. From the 90° angle, it can be observed that the thin IP-S layer, indicated by the arrows, is still visible but less defined and even partially detached from the substrate. In the bottom view, it is evident that the IP-S layer is significantly reduced, with almost no remaining contrast.

The results of increased membrane thickness and height are shown in Figure 4.19. Here, even after the plasma asher process step, the membranes upheld their planar structure.

Limitations of IP-S removal with the plasma asher in this case may be that the IP-S membranes are shielded by the GP-Silica on the outside. However, even in areas where the GP-Silica membranes do not cover the IP-S, some residues remain.

Another possible limiting factor is that GP-Silica resin leaves residues wherever unpolymerized resin was present during the printing process. Therefore, it is likely that some glass particles are left on the IP-S membranes as well, which could passivate the organic IP-S layer against the oxygen radicals from the plasma asher.

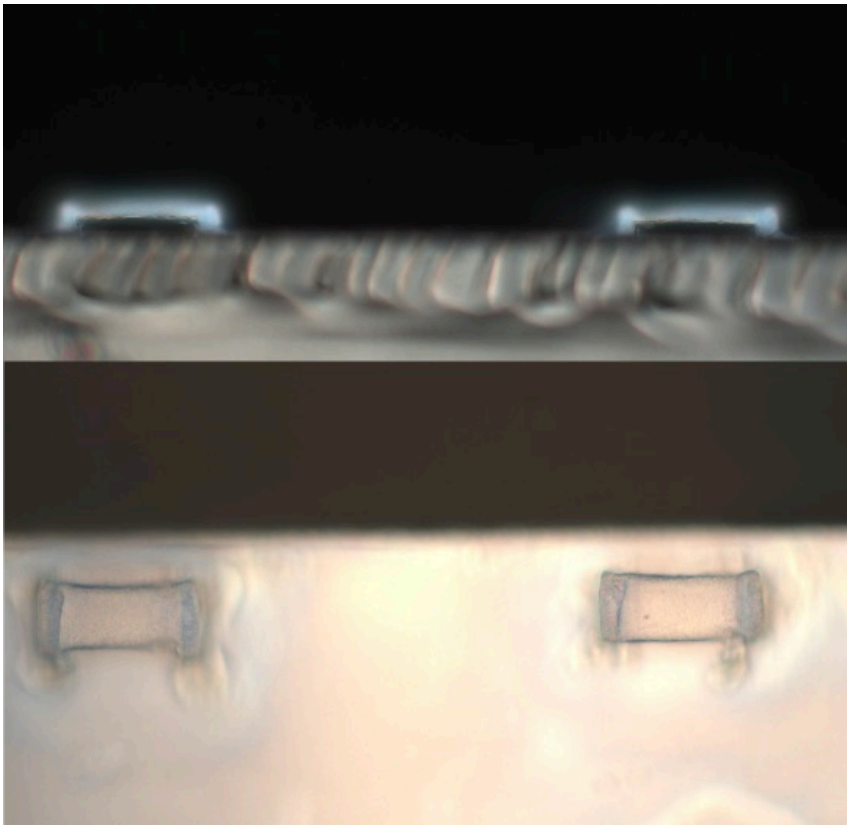

Figure 4.19: In this image, the results are shown for membranes with an increased height from 10 $\mu m$ to 19 $\mu m$ and a thickness of 2.5 $\mu m$, which were plasma ashed at 100% power for two hours. The top image, taken from a 90° angle with the focus on the IP-S layer, shows that the layer is reduced in thickness while the membranes remain planar. The bottom image, taken from a top-down perspective, reveals the roughly homogeneous surface of the GP-Silica membrane and that the contrast of the IP-S membrane is significantly reduced.

The sintering process of the combined membranes is challenging due to the requirement for a large shot radius and the need for the shots to be homogeneous, meaning a very flattened Gaussian beam profile. The beam radius must be uniform within at least 60 $\mu m$. In order to get a tendency for the correct shooting parameters for the combined membranes, a large parameter variation was carried out, which can be seen in Figure 4.20, here it becomes clear that simply moving out of focus does not directly solve the problem.

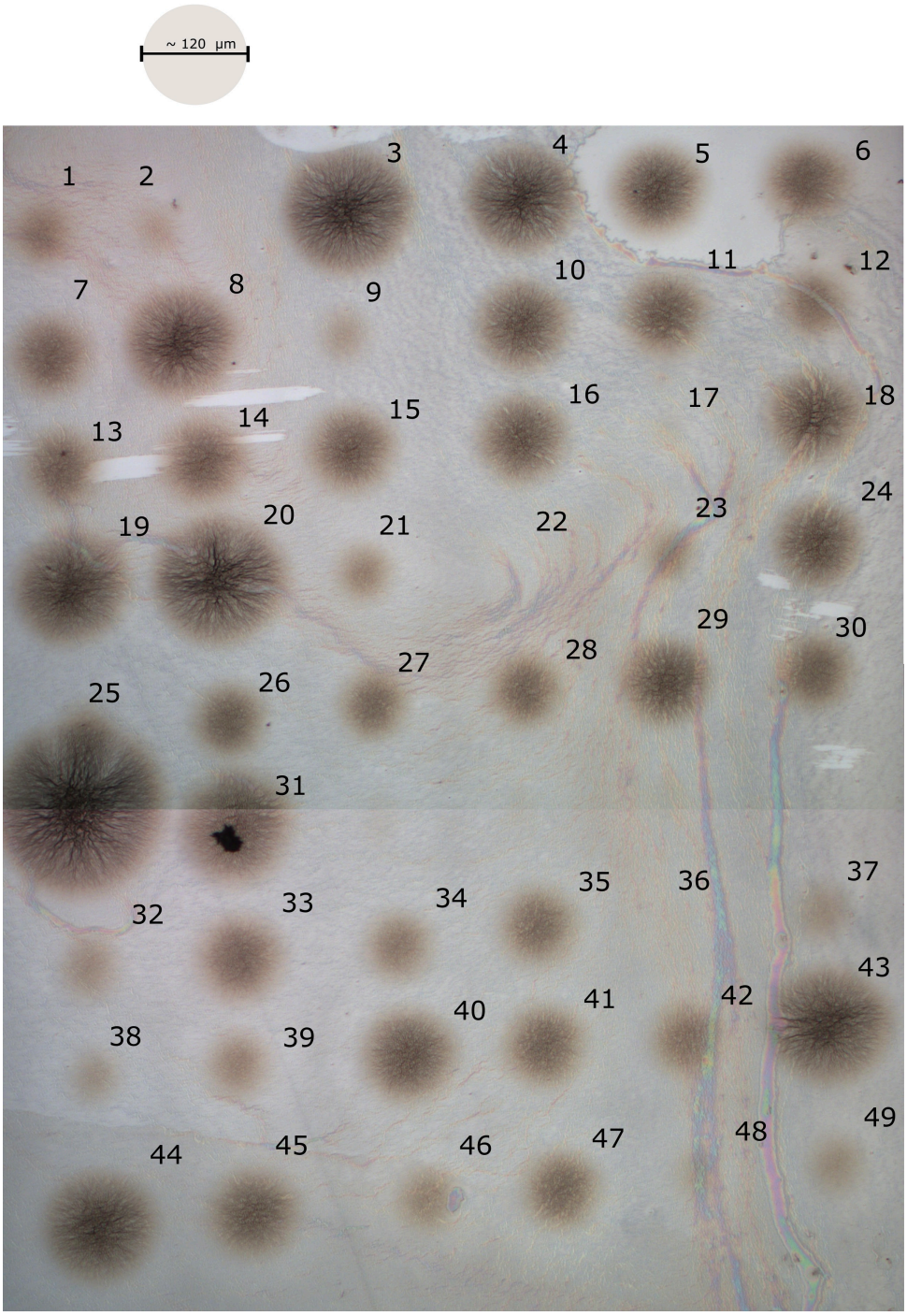


Figure 4.20: In this picture, the variation of shooting parameters on an ITO substrate for shots far from the laser beam focus, with $y_{\text{diff}} = 1\,mm$ and $0.5\,mm$, is shown. At the top, a schematic, drawn to the same scale, illustrates the required shot size for the $120 \times 50\,\mu m$ GP-silica membranes. It can be observed that when the shot radius reaches approximately $60\,\mu m$, the substrate's structure changes due to the exposure. This indicates that such a shot would likely be too strong for the fragile membranes to maintain their shape during sintering. The corresponding shooting parameters are listed in Table A.4.

In Figure 4.21, the results of the first sintering tests of the combined membranes can be seen. Either the membranes burst in the middle due to thermal pressure and potentially radiation pressure (with the shooting parameters: $\tau$= 44 ms, n= 54, $P_0$=3.5 W, Fraction AOM (%): 0.2:0.4:0.6:0.8:1:0.8:0.6:0.4:0.2, $\Delta\tau$= 86 ms, $y_{\text{diff}}$= 0.5 mm), or the structure did not change in its form (from a top-down-perspective) or

optical properties, which leads to the interpretation that the structures were not sintered at all. However, at this stage, the applied dose is potentially still too low to fully sinter the membranes.

From a 90° angle (see Figure 4.21), it is noticeable that the membranes bend toward the substrate after getting shot. In the light microscope, it is expected that the membranes should decrease in contrast and become more transparent after successful sintering.

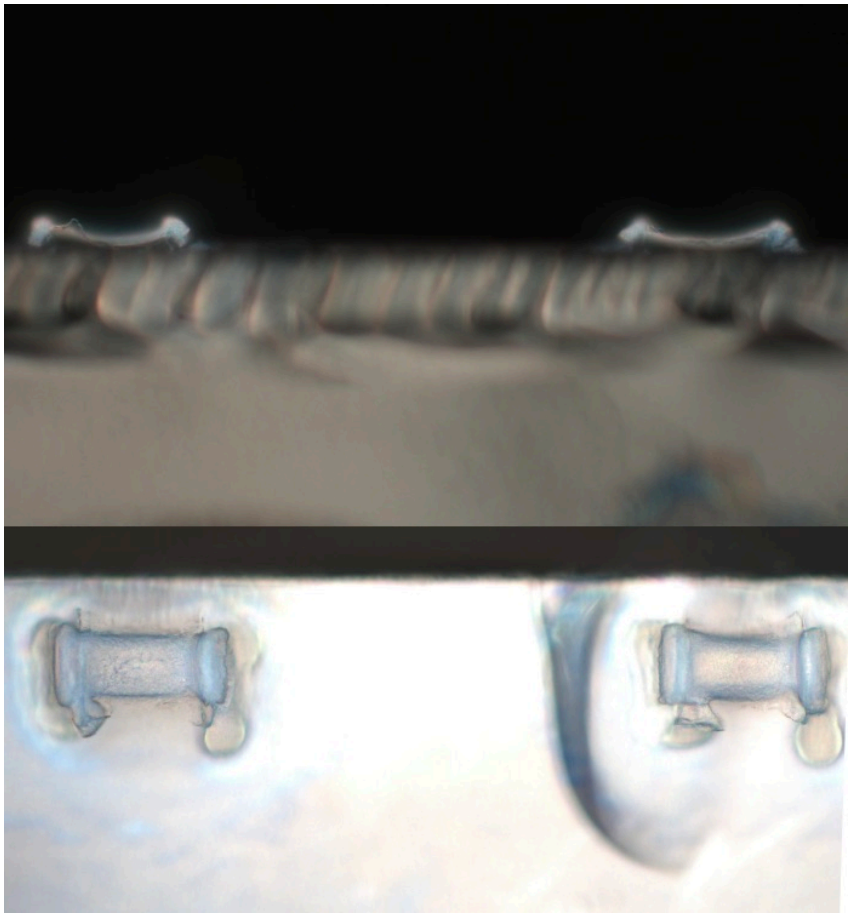

Figure 4.21: In this image, combined membranes that were plasma-ashed prior to shooting are shown, once from a 90° angle (*top*) and once from a top-down perspective (*bottom*). From the 90° perspective, the remnants of the IP-S membranes appear as thin, transparent, frayed layers, visible in focus on the left membrane. Additionally, the membranes have been pressed down at the center to the substrate, whereas they were planar before. From the top-down perspective, it can be observed that the optical properties have not changed significantly after shooting, and there are no indications of membrane contraction. Based on these observations, it can be concluded that the membranes were not fully, or possibly not at all, sintered.

The fluctuations of the laser power in this shooting setup are on the order of 10%. In Figure 4.22, one can see the difference these laser power variations make for the small, fragile membranes. The corresponding shooting parameters can be found in Table 4.1.

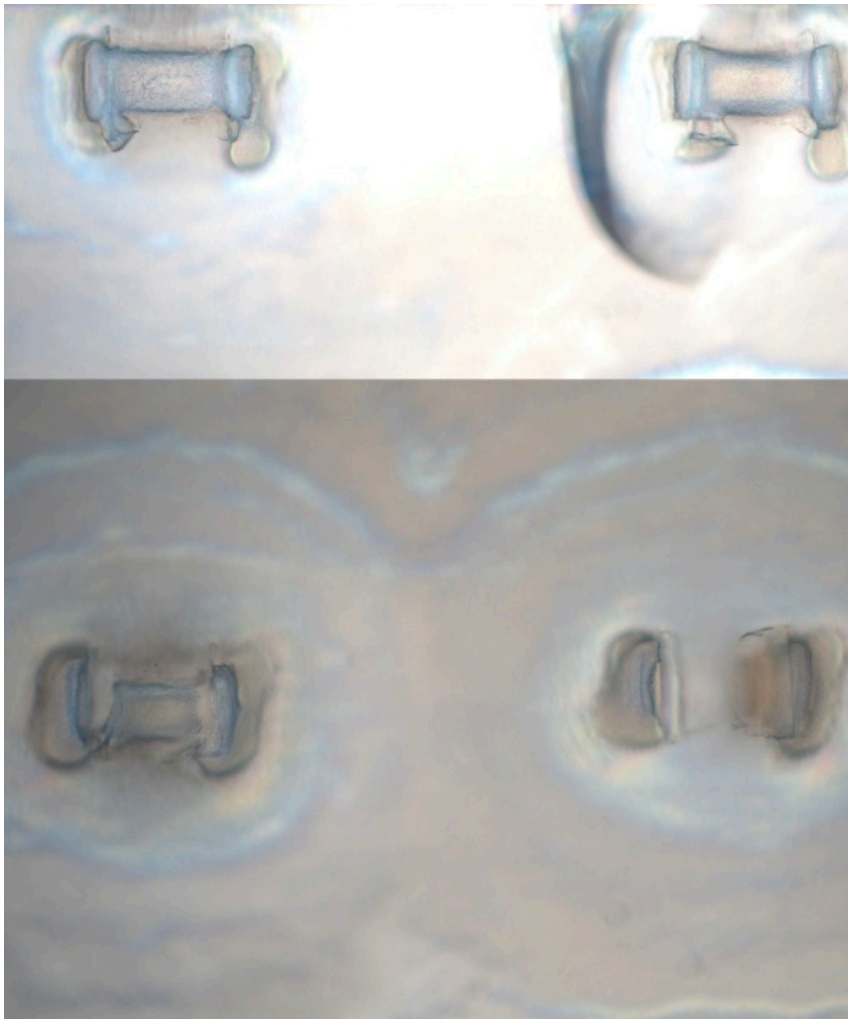

Figure 4.22: In this image, the top row shows two membranes that were shot with the same maximum laser power of 3.5 $W$. These membranes appear to be largely intact. In contrast, the bottom row shows two membranes that were destroyed. The maximum laser power set for the shots to these membranes was 3.6 $W$, even though the shot duration was reduced by approximately 10% compared to the membranes in the top row.

| Start (W) | End (W) | Label | $\tau$ (ms) | n | $P_0$ (W) | AOM Profile (%) | $\Delta\tau$ (ms) | $y_{\text{diff}}$ (mm) |
|---|---|---|---|---|---|---|---|---|
| 3.663 | 3.655 | bridge(top,left) | 45 | 54 | 3.5 | 0.2:0.4:0.6:0.8:1:0.8:0.6:0.4:0.2 | 85 | 0.5 |
| 3.659 | 3.661 | bridge(top,right) | 46 | 54 | 3.5 | 0.2:0.4:0.6:0.8:1:0.8:0.6:0.4:0.2 | 83 | 0.5 |
| 3.855 | 3.853 | bridge(bottom,left) | 40 | 54 | 3.6 | 0.2:0.4:0.6:0.8:1:0.8:0.6:0.4:0.2 | 80 | 0.5 |
| 3.850 | 3.851 | bridge(bottom,right) | 40 | 54 | 3.6 | 0.2:0.4:0.6:0.8:1:0.8:0.6:0.4:0.2 | 80 | 0.5 |

Table 4.1: Shot parameters of Figure 4.22: start and end values refer to the measured power before and after the shot. It can be observed that the difference between the set laser powers of 0.1 $W$ is smaller than the difference between the nominal and the actual applied power in one shot, which in this case is up to 0.255 $W$. This difference is sufficient to determine whether the membranes are destroyed or remain intact, indicating that the inaccuracy of the shooting setup is therefore a critical factor.

Another approach that could stabilize the membranes during the sintering process would be to remove the IP-S membrane either after or during the sintering process. The IP-S resin is not designed to be sintered and will eventually burn [24]. In Figure 4.23, an IP-S membrane that was shot with the $CO_2$ laser is shown. It is noticeable that the IP-S almost completely vanishes, leaving only minimal residue, a small, crumbled leftover tissue that appears dark. This is potentially a favorable result. If the IP-S had shattered, the GP-Silica membranes would likely have been contaminated during sintering by soot originating from the burned IP-S. However, this result is not directly transferable to the combined membranes, as the

behavior of IP-S in contact with GP-Silica could differ substantially from that of a free-standing IP-S membrane and could therefore still lead to contamination of the GP-Silica membranes.

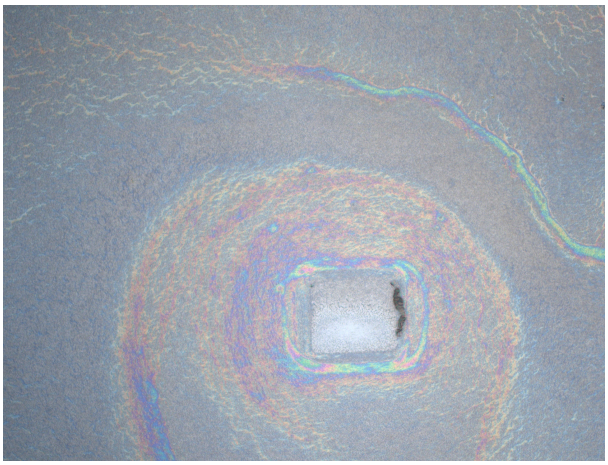

Figure 4.23: The result of shooting an IP-S membrane with a thickness of 2.5 $\mu$m using the parameters $\tau$ = 45 ms, $n$ = 36, $P_0$ = 3 W, Fraction AOM (%): 0.2:0.4:0.6:0.8:1:0.8:0.6:0.4:0.2, $\Delta\tau$ = 50 ms, and $y_{\text{diff}}$ = 1 mm is shown. The material appears burned, as indicated by the change in color from bright beige (see previous images of IP-S membranes) to a darker brown. At the right side, the membrane has crumbled into small pieces. The area where the membrane was originally located is visible because the GP-Silica stained the substrate. This occurred because the substrate was exposed to GP-Silica. The IP-S membrane was part of an array in which the other membranes were developed into combined membranes, whereas this particular one consisted solely of IP-S.

The results of shooting on the combined membranes using the same shooting parameters, but without the previous plasma asher process, are shown in Figure 4.24. It is noticeable that the bending gets prevented. However, the right shooting-parameters are not found yet, because the membranes are not transparent and therefore probably not sintered fully.

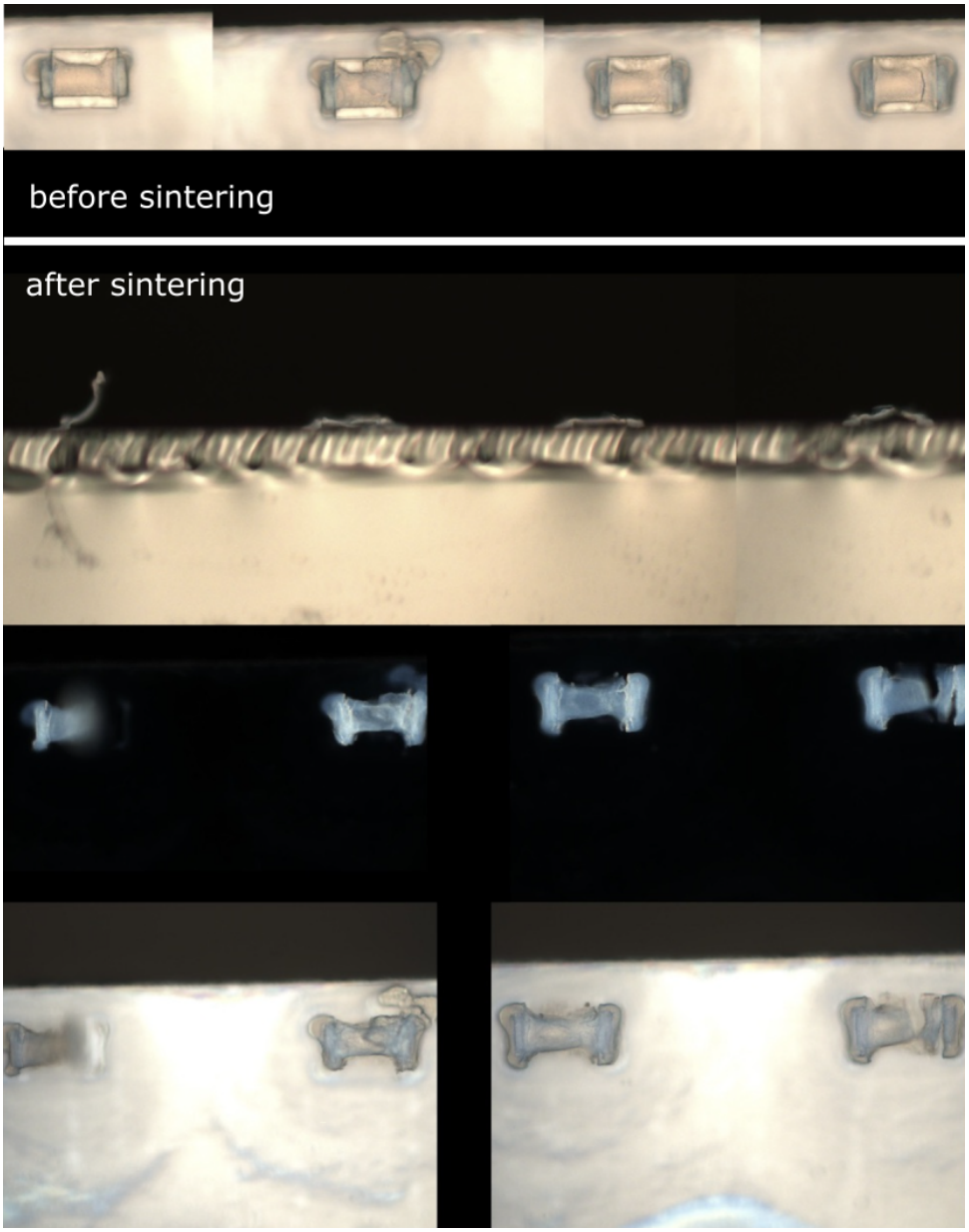


Figure 4.24: In this image, at the top, combined printed membranes are shown which were not plasma-ashed prior to sintering. Therefore, the IP-S membranes are not reduced in size and provide support to the GP-Silica membranes from underneath. The same membranes were subsequently sintered (see shooting parameters in A.2) and afterwards plasma-ashed. The results are shown from a 90° angle, followed by a top-down perspective in dark-field mode, and finally in bright-field mode at the bottom to estimate the degree of sintering. From the 90° perspective, it can be seen that the second and third membranes are not destroyed, and in this case they are not bent towards the substrate, in contrast to the previously plasma-ashed membranes prior to sintering. From the top-down perspective in both imaging modes, the membranes do not exhibit the optical properties characteristic of sintered GP-Silica: their transparency has not increased in dark-field, and in bright-field they show no significant shrinkage compared to unsintered membranes, as would be expected during successful sintering.

To achieve better shooting results, it is advisable to reduce the size of the structures. It is simpler to shoot smaller radii because increasing the distance to the focus point of the laser beam reduces the power density. To compensate and reach higher power levels, one can increase the number of pulses and the duration of each pulse. The shots also have a stronger effect on both the substrate and the structures when the delay between the pulses is reduced. A possible explanation for this observation is that in this case, the elevated temperature caused by one pulse does not have time to dissipate into the surrounding material before the next pulse arrives.

This thermal accumulation effect is smaller than the impact of increasing the number of pulses or increasing the pulse duration (for this shoot button and this profile, it may vary with different profiles). However, the longer the total shot sequence becomes, due to a high number of long pulses, the more the synchronization between software and hardware deteriorates.

It is also possible to reach the required dose by simply increasing the maximum power used. However, if the sample is placed multiple Rayleigh lengths away from the focus point, the power needs to be increased to a level where the calibration of the AOM and the power meter becomes inaccurate. Figure 4.25(a) and 4.25(b) visualizes that the calibration shows a higher deviation beginning at a voltage of 3 V.

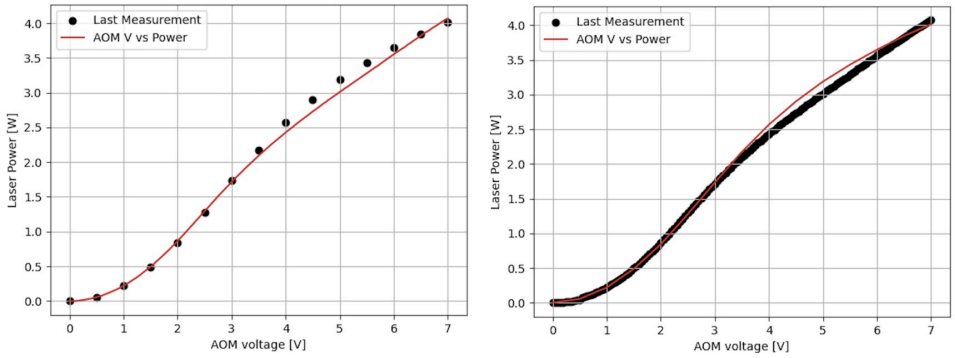


(a) Calibration with 1 s waiting time. *Left*: calibration in 0.05 V steps, where the measured laser power above 3 V is lower than expected. *Right*: calibration in 0.5 V steps, where the measured laser power is higher than expected.

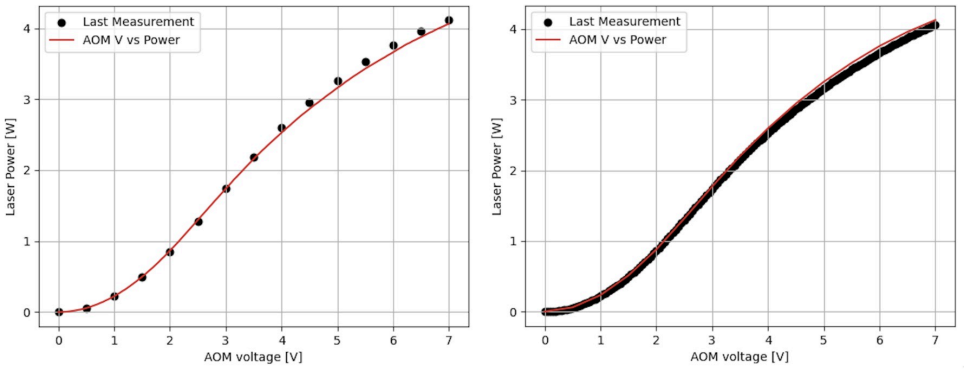


(b) Calibration with 2 s waiting time. The increased waiting time results in a more accurate calibration, even above 3 V.

Figure 4.25: Comparison of calibration curves for different waiting times between measurements. The calibration curves are obtained by plotting the measured laser power against the AOM voltage and adjusting to align the set laser power with the actual applied power.

This problem was resolved by making a small adjustment in the Python script that controls the shooting setup. In this modification, the time between the calibration measurements was changed from 1 second to 2 seconds. The increased interval between calibration pulses better mimics the actual shooting process and results in a more reliable laser power calibration, even for higher laser power values. The laser power is not linear. The deviation from linearity increases when using higher power values from 1–4 W. The laser power behaves much more linearly in the lower power range of 0.01–1 W.

These two limitations concerning the needed laser power can be avoided by placing the sample closer to the focus point, where the laser power reaches its maximum value. This reduces the radius in which the shot remains homogeneous. As mentioned before the homogeneity is essential for sintering membranes without imprinting the Gaussian profile into them. Therefore, smaller combined membranes are a rational approach.

In Figure 4.26, results are shown for a combined membrane print with a $50 \times 88$ $\mu$m GP-Silica membrane.

The membranes exhibit less leakages, cracks and are roughly planar. These membranes were not subjected to plasma ashing due to the instability issues during sintering mentioned earlier. Membranes from this array were sintered using shooting parameters similar to those applied to the $50 \times 50\,\mu$m cubes with a height of $2.5\,\mu$m, and the results are shown in Figure 4.27[2]. Here the Laserpower can be decreased down to $\sim 0.3\,W$, due to the smaller required homogeneous shooting radius, which enables finer controlling of the laserpower. The results show, that the membranes exhibit increased transparency in dark-field mode and also brightened optical properties in bright-field, therefore the membranes are likely fully sintered and the IP-S membrane is no longer visible.

At this stage, with a short printing duration and therefore fewer leakages, and using the same shooting parameters, the membranes already appear optically quite good. In summary, they are stable, upright, free of cracks, and very likely fully sintered without bending or sagging to the substrate. The next step would be to print these membranes onto a mirror and investigate their mechanical properties. Furthermore, it must be ensured that the substrate, and later the mirror, are clean beneath the membranes. It is likely that streaks of GP-silica remain under the membranes as well. Here, methods must be explored to remove them without detaching the structures themselves.

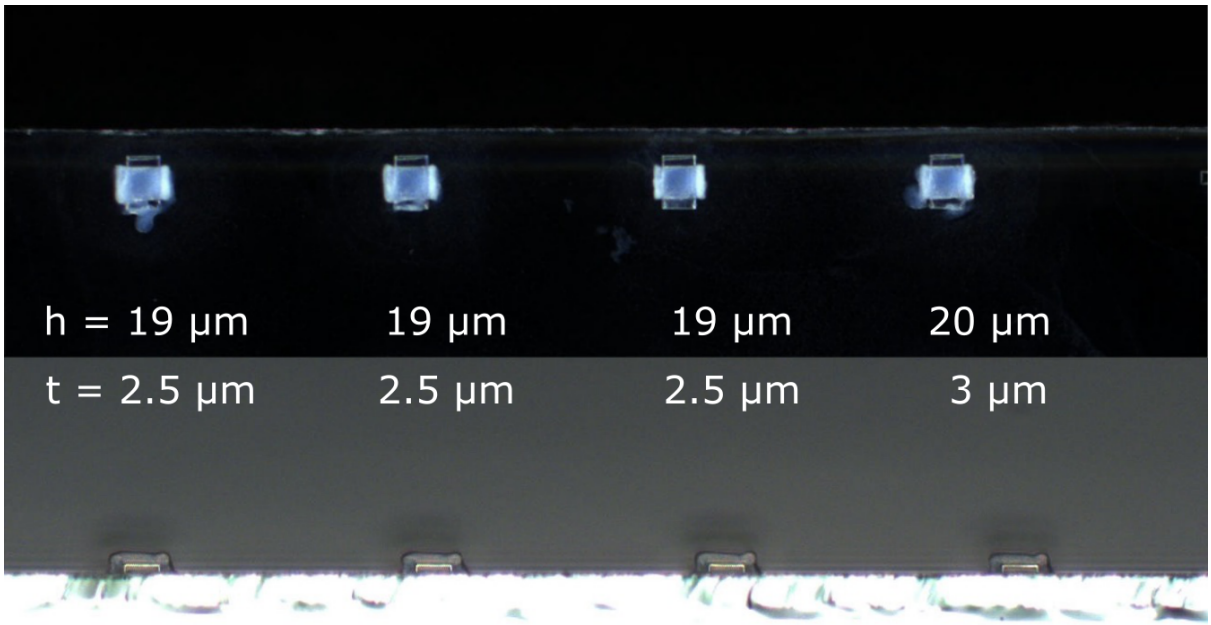


Figure 4.26: The result of printing the $90 \times 50\,\mu$m (IP-S) $50 \times 88\,\mu$m (GP-Silica) combined membrane is shown. *Top*: top-down perspective; *bottom*: 90° angle view. The membranes appear stable without major defects. From the 90° perspective, it is also visible that they are planar and that the gap is maintained.

[2] The leakages, appear in the printing/developing process not in the sintering process, the membranes from 4.27 and 4.26 are not the same but from the same array with relatively small thickness and height variations

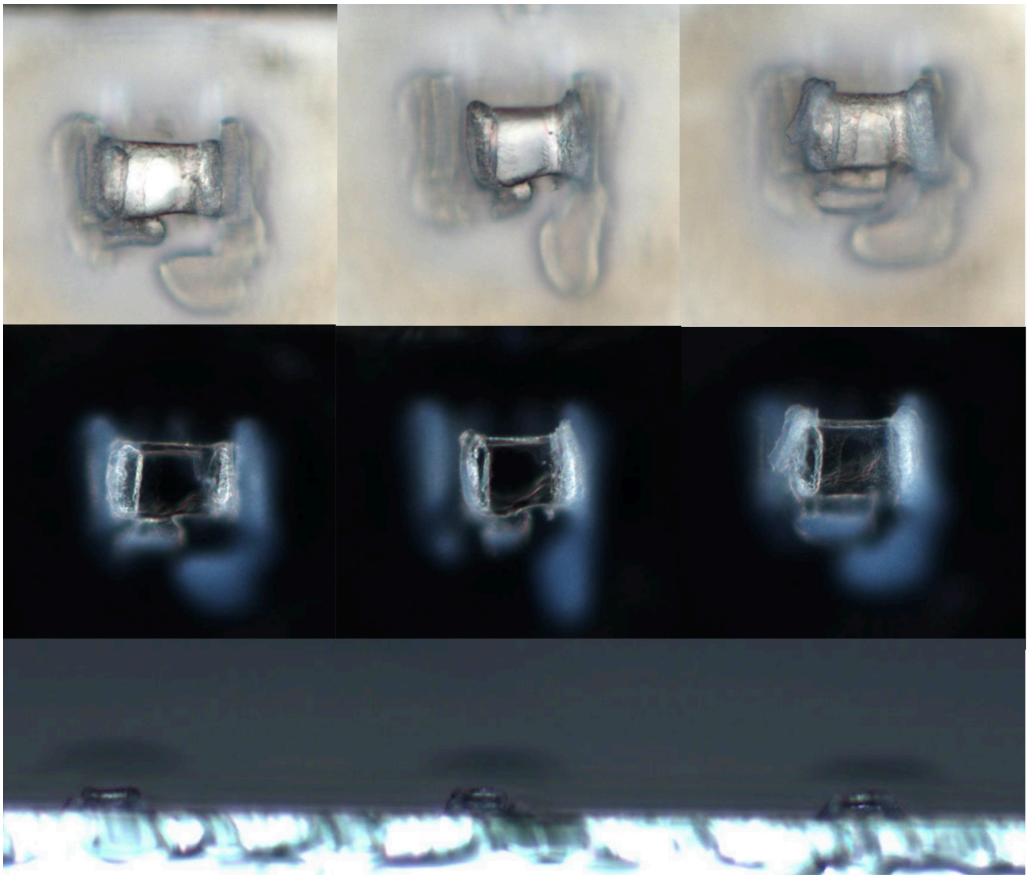

Figure 4.27: The result of sintering the $50 \times 88\,\mu$m (GP-Silica) ( $90 \times 50\,\mu$m(IP-S)) combined membrane is shown. *Top*: top-down perspective bright-field, *Center*: top-down perspective dark-field, *Bottom*: 90° angle view. The shooting parameters used can be seen in A.3. The transparency of the membranes increased in dark-field imaging, while their overall shape remained largely unchanged except for the shrinkage. From a 90° viewing angle, the membranes also appear to preserve their shape, and the gap between the substrate and the membrane is maintained as well.

CHAPTER 5

# Conclusion

While the goal of fully optimizing the fabrication of two-photon 3D-printed, laser-sintered GP-silica membranes was not entirely achieved, this work led to the identification of several critical issues and limitations in the current process, thereby providing a valuable foundation for future improvements.

The first reproduction prints showed that the GP-silica resin degrades over time (developing very low resolution and leakage defects). In this case, this occurred six months after opening the cartridge. As a result, the reproduction of previous results required additional effort. With fresh GP-silica resin, it was possible to reproduce the previous results. However, when reproducing the sintering experiments, it was observed that the structures likely did not become thoroughly sintered. In the search for new shooting parameters, a new Python function was implemented to vary the pulse profile, since the previous version showed some flaws. Optimized parameters for sintering cubes were first established, as cubes represent simpler structures suitable for evaluating the optical properties of GP-silica.

Another goal of this work was to measure the optical finesse of laser-sintered GP-silica cubes. It was found, however, that the optical surface of the underlying mirror was heavily contaminated after prints with GP-silica, rendering a rigorous measurement impossible. This contamination could not be easily removed, as the printed structures detached before effective cleaning could be achieved. This goal was therefore not accomplished. Many cleaning methods were tested, including ultrasonic baths with NMP and isopropanol[1], both with and without nitrogen blow-off, plasma ashing, mechanical motion, and various durations of development in methanol. Even when the structures were fully sintered or partially melted, they detached earlier than the residues when subjected to these cleaning methods. Therefore, residues should be prevented in advance. It was found that shortening the printing duration decreases the occurrence of residues.

Measuring the coupling depth with the VFM, large optical losses were observed, but a trend was found toward higher coupling depths in more glass-like structures. Another obstacle in measuring the coupling depth is that the surfaces of the sintered structures were likely not sufficiently planar. This issue could potentially be resolved by further defocusing the laser beam, such that the sintering shots are less sensitive to precise centering on the structure. However, this would require the use of a finely tunable laser with output powers up to 4 W. The $CO_2$ laser setup used here exhibits strong fluctuations at such high powers. Another idea is to sinter the structures in an oven. This would ensure homogeneous shrinkage of the structures. To avoid the problem that the mirrors cannot withstand the required temperatures, one possible solution might be to print and sinter the structures separately on a substrate and later on transfer them onto the mirror. This approach, however, would eliminate the strain introduced when the structures are printed directly onto the mirror surface. This strain has been shown to enhance the Q-factor; more information on this topic can be found in [7]. Because of the already high Q-factor of GP-silica, this could still be an interesting idea.

Focusing on the membrane printing, the following observations were made, the main evaluation tool, the optical microscope, was insufficient. This was already a problem in previous work, since the structures

[1] The latter is recommended by Nanoscribe for removing GP-silica structures from a substrate, although they note that force may be required, and their recommendation applies primarily to larger structures [20].

were judged solely from a top-down perspective. By viewing the samples from the side in this thesis, however, more information could be obtained. It was found that the previous printing technique failed to produce suspended structures.

A new printing technique was therefore developed, that makes use of an additional IP-S support structure to stabilize the GP-silica during printing and ensure its structural integrity. First, an IP-S membrane in a table-like geometry was printed, and then the GP-silica membrane was printed on top of the IP-S support. The IP-S structure supported the weight of the GP-silica membrane, which otherwise tends to collapse under its own weight.

Initial tests on the removal of the support structures were carried out. While the IP-S was not completely removed, insight was gained into possible refined printing strategies and removal techniques. The removal of the IP-S membrane beneath the GP-silica membrane was not successful using plasma ashing. Instead sintering the combined membranes without any prior efforts of removing the IP-S support lead to more promising results. After the sintering of the GP-Silica the IP-S seemed to be removed when observing the samples with the light microscope. Nevertheless this should be further investigated since no further evaluation was carried out to confirm a full removal. By decreasing the size of the membranes and using similar shooting parameters as for comparably sized cubes, it was possible to seemingly achieve fully sintered membranes with reasonably good optical properties. The next step of this project would be to print these membranes onto a mirror to investigate their mechanical properties.

# APPENDIX A

## Figures:

```python
def shoot_button2(self):
        """ Sets the shooting voltage waveform to the BNC board"""

        # initialise a ni task, ni = NationalInstruments (data aquisition task)
        # here we initialise 3 tasks and name them
        with ni.Task() as analogue_task, ni.Task() as trig_task, ni.Task() as gate_task:
            print("Shooting...", end = "\r")
            # Calculated shooting time + some extra seconds for time out control
            time_for_shooting=int(self.no_of_pulses*(self.delay_bw_pulses+self.pulse_duration)+30)
            print("parameters to check")
            print(self.no_of_pulses)
            print(self.pulse_duration)
            print(self.delay_bw_pulses)

            analogue_task.ao_channels.add_ao_voltage_chan(self.analog_channel_aom)
            trig_task.co_channels.add_co_pulse_chan_time(self.trig_chan_generation, high_time=self.pulse_duration, low_time=self.delay_bw_pulses)#
            gate_task.co_channels.add_co_pulse_chan_time(self.digital_channel_aom_shoot, high_time=self.pulse_duration, low_time=self.delay_bw_pulses)#
            print("Test i am here")

            #data=self.sample_pulse(self.pulse_duration, self.delay_bw_pulses, self.aom_voltage)

            #-----------------------------------------------------------------------------------------------------------------------------------------------

            # --> array of amplitudes that are written over a duration of "puls duration"
            self.samples_per_second = 500000


            # Creat an empty list of amplitudes:
            amps_for_writing = []

            # Create the function for creating a high or low
            def create_a_low():
                for i in range(0, length_of_a_low+1,1):
                    amps_for_writing.append(0)

            def create_a_high(fraction):
                for i in range(0, length_of_a_high+1, 1):
                    amps_for_writing.append(self.aom_voltage*fraction)
```

```python
            # Create the first (of many) highs, + some variables
            fraction_list = [0.2, 0.4,0.6,0.8, 1,0.8,0.6, 0.4,0.2]
            length_of_a_high = int(self.pulse_duration * self.samples_per_second)
            length_of_a_low = int(self.delay_bw_pulses * self.samples_per_second)

            pulses = []
            for fraction in fraction_list:
                print(fraction)
                lows = np.zeros(length_of_a_low)
                highs = np.ones(length_of_a_high)*self.aom_voltage*fraction
                one_puls = np.concatenate((lows, highs))
                pulses.append(one_puls)

            pulses.append(np.zeros(length_of_a_low))

            pulses = np.concatenate(pulses, axis = 0)

            # Creating an array out of the list
            amps_for_writing = pulses

            plt.plot(pulses[::1000])
            plt.show()

            amps_for_writing = np.array(amps_for_writing)

            print("Delay", self.delay_bw_pulses)
            print("Rate", self.samples_per_second)
            #-----------------------------------------------------------------------------------------------------------------------------------------------


            # Definition of task timings: Writing with a rate of "samples per second" a certain amount of samples (samps_per_chan)
            analogue_task.timing.cfg_samp_clk_timing(rate = self.samples_per_second,samps_per_chan=self.no_of_pulses*len(amps_for_writing))
            trig_task.timing.cfg_implicit_timing(sample_mode=AcquisitionType.FINITE, samps_per_chan=1)
            gate_task.timing.cfg_implicit_timing(sample_mode=AcquisitionType.FINITE, samps_per_chan=self.no_of_pulses)
            analogue_task.triggers.start_trigger.cfg_dig_edge_start_trig(trigger_source=self.trig_source)
            gate_task.triggers.start_trigger.cfg_dig_edge_start_trig(trigger_source=self.trig_source)
            analogue_stream = AnalogSingleChannelWriter(analogue_task.out_stream)
```

```python
            # Actual writing of samples:
            samples_written = analogue_stream.write_many_sample(amps_for_writing)
            print("Number of written samples:", samples_written)
            analogue_task.start() # start the writing process
            gate_task.start()
            trig_task.start()

            print("Time for Shooting test:", time_for_shooting)
            analogue_task.wait_until_done(timeout= WAIT_INFINITELY)
            trig_task.wait_until_done(timeout=WAIT_INFINITELY)
            print("Shooting Done, Time for Shooting:", time_for_shooting)
```

Figure A.1: The figure shows the code of the new shoot button, extracted from the Python script that operates the shooting setup.

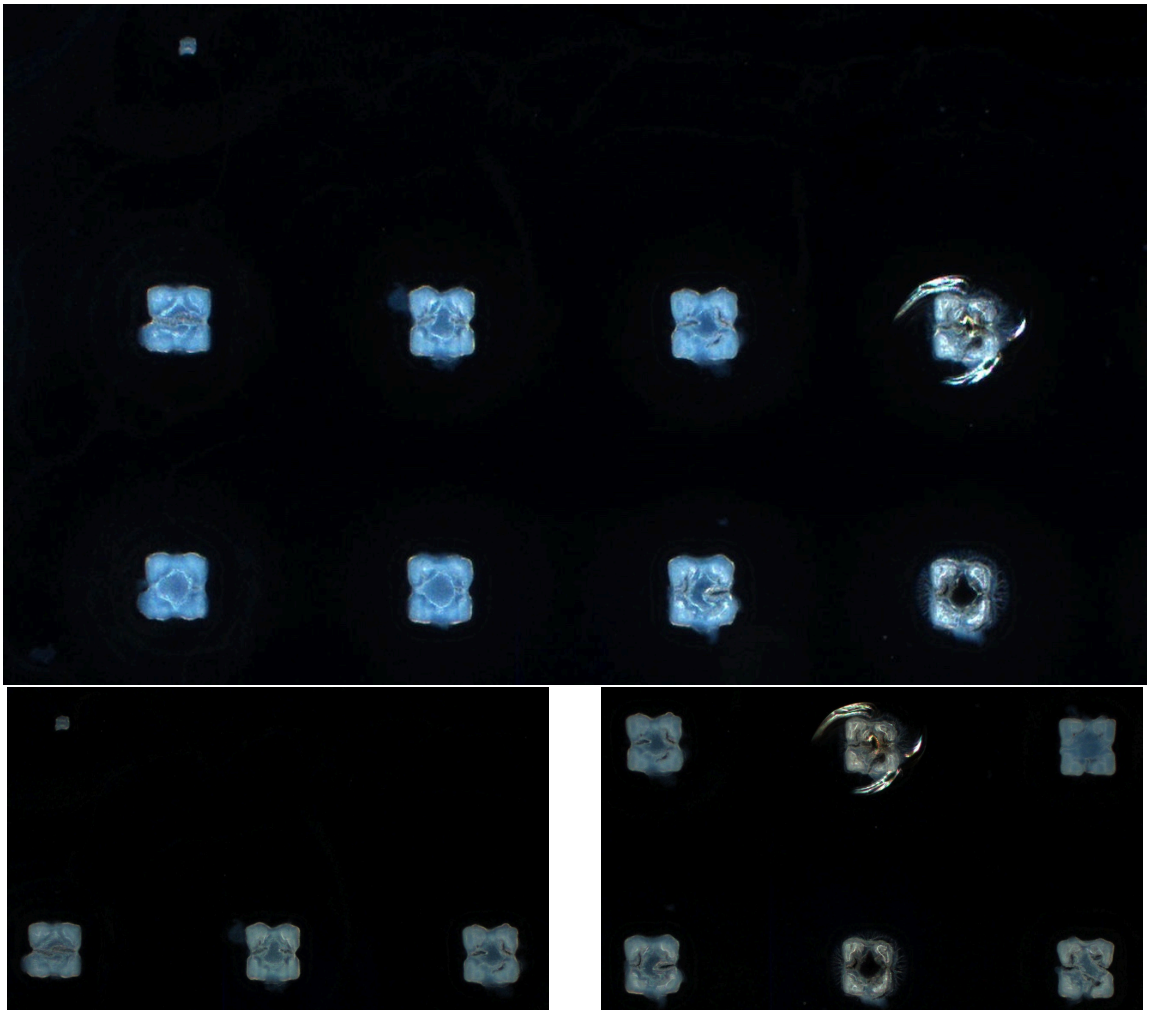

Figure A.2: In this figure, the *top* image shows an array of membranes that were partially sintered. The marker visible at the top was not shot. The *bottom* image shows the same array after one hour of plasma ashing at 100% power. The marker remains visible, and the membranes did not exhibit any noticeable changes.

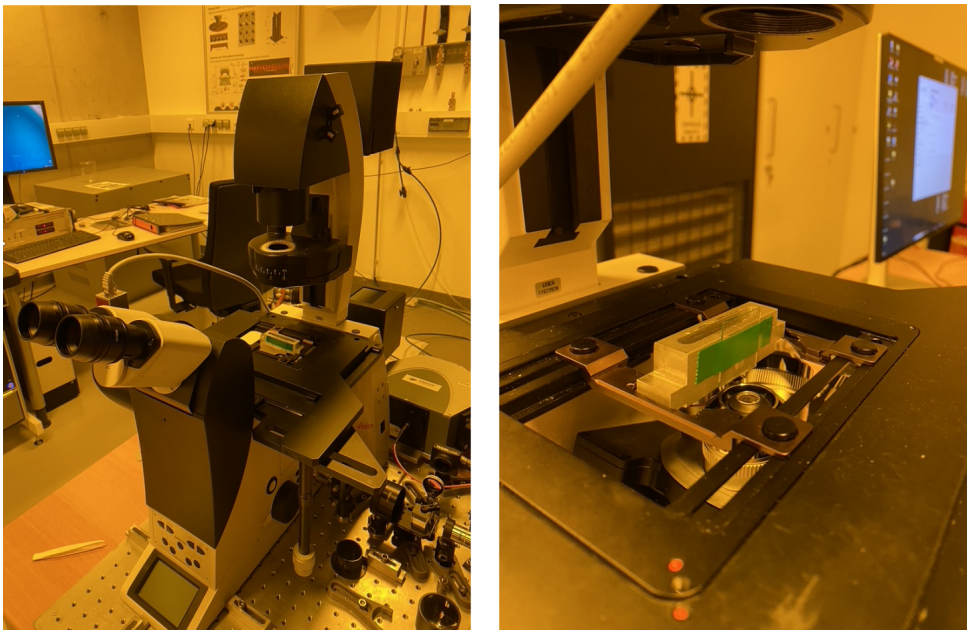

Figure A.3: In the image, the LEICACTR4000 microscope is shown,which was used in addition to the main light microscope, to observe the membranes from a 90° perspective.

## Tables:

Table A.1: Shooting parameters of Figure 3.2(b): pulse duration $\tau = 8\,\text{ms}$, $y_{\text{diff}} = 5.775\,\text{mm}$, using the previous shooting button for initial results.

| membrane | number of pulses | pulse | AOM voltage (%) | laserpower $P_0$ (W) |
|---|---|---|---|---|
| 1 | 10 | 1–2 | 50 | 0.15 |
| | | 3–8 | 100 | |
| | | 9–10 | 50 | |
| 2 | 10 | 1–2 | 50 | 0.20 |
| | | 3–8 | 100 | |
| | | 9–10 | 50 | |
| 3 | 10 | 1–2 | 50 | 0.25 |
| | | 3–8 | 100 | |
| | | 9–10 | 50 | |
| 4 | 10 | 1–2 | 50 | 0.30 |
| | | 3–8 | 100 | |
| | | 9–10 | 50 | |
| 5 | 10 | 1–2 | 50 | 0.40 |
| | | 3–8 | 100 | |
| | | 9–10 | 50 | |
| 6 | 10 | 1–2 | 50 | 0.50 |
| | | 3–8 | 100 | |
| | | 9–10 | 50 | |

Table A.2: Shooting parameters for the four bridges from Figure 4.24. “Start” and “End” indicate the laser power measured before and after the shot. From left (1) to right (4).

| Start (W) | End (W) | Bridge | $\tau$ (ms) | $n$ | $P_0$ (W) | Fraction AOM (%) | $\Delta\tau$ (ms) | $y_{\text{diff}}$ (mm) |
|---|---|---|---|---|---|---|---|---|
| 3.747 | 3.911 | bridge1 | 44 | 54 | 3.8 | 0.2:0.4:0.6:0.8:1:0.8:0.6:0.4:0.2 | 86 | 0.5 |
| 3.522 | 3.629 | bridge2 | 44 | 54 | 3.8 | 0.2:0.4:0.6:0.8:1:0.8:0.6:0.4:0.2 | 86 | 0.5 |
| 3.452 | 3.449 | bridge3 | 44 | 54 | 3.8 | 0.2:0.4:0.6:0.8:1:0.8:0.6:0.4:0.2 | 86 | 0.5 |
| 3.445 | 3.247 | bridge4 | 44 | 54 | 3.5 | 0.2:0.4:0.6:0.8:1:0.8:0.6:0.4:0.2 | 86 | 0.5 |

Table A.3: Shooting parameters of the sintering results shown in Figure4.27. From left (1) to right (3).

| Bridge | $\tau$ (ms) | $n$ | $P_0$ (W) | Fraction AOM (%) | $\Delta\tau$ (ms) | $y_{\text{diff}}$ (mm) |
|---|---|---|---|---|---|---|
| bridge1 | 30 | 36 | 0.35 | 0.2:0.4:0.6:0.8:1:0.8:0.6:0.4:0.2 | 50 | 4.2 |
| bridge2 | 30 | 36 | 0.35 | 0.2:0.4:0.6:0.8:1:0.8:0.6:0.4:0.2 | 50 | 4.2 |
| bridge3 | 30 | 36 | 0.30 | 0.2:0.4:0.6:0.8:1:0.8:0.6:0.4:0.2 | 50 | 4.2 |

Table A.4: Shooting parameters using the new shoot button from the parameter variation, aiming to identify a parameter set in which the radius is sufficiently large and homogeneous. From Figure 4.20.

| Messung | $\tau$ (ms) | n | $P_0$ (W) | Fraction AOM (%) | $\Delta\tau$ (ms) | $y_{\text{diff}}$ (mm) |
|---|---|---|---|---|---|---|
| 1 | 45 | 36 | 3.00 | 0.2:0.4:0.6:0.8:1:0.8:0.6:0.4:0.2 | 20 | 1.0 |
| 2 | 45 | 36 | 3.00 | 0.2:0.4:0.6:0.8:1:0.8:0.6:0.4:0.2 | 30 | 1.0 |
| 3 | 45 | 36 | 3.10 | 0.2:0.4:0.6:0.8:1:0.8:0.6:0.4:0.2 | 2 | 1.0 |
| 4 | 45 | 36 | 3.10 | 0.2:0.4:0.6:0.8:1:0.8:0.6:0.4:0.2 | 4 | 1.0 |
| 5 | 45 | 36 | 3.10 | 0.2:0.4:0.6:0.8:1:0.8:0.6:0.4:0.2 | 6 | 1.0 |
| 6 | 45 | 36 | 3.10 | 0.2:0.4:0.6:0.8:1:0.8:0.6:0.4:0.2 | 8 | 1.0 |
| 7 | 45 | 36 | 3.10 | 0.2:0.4:0.6:0.8:1:0.8:0.6:0.4:0.2 | 10 | 1.0 |
| 8 | 45 | 36 | 3.00 | 0.2:0.4:0.6:0.8:1:0.8:0.6:0.4:0.2 | 4 | 1.0 |
| 9 | 45 | 36 | 2.60 | 0.2:0.4:0.6:0.8:1:0.8:0.6:0.4:0.2 | 4 | 1.0 |
| 10 | 45 | 36 | 2.90 | 0.2:0.4:0.6:0.8:1:0.8:0.6:0.4:0.2 | 4 | 1.0 |
| 11 | 45 | 36 | 2.80 | 0.2:0.4:0.6:0.8:1:0.8:0.6:0.4:0.2 | 4 | 1.0 |
| 12 | 45 | 36 | 2.70 | 0.2:0.4:0.6:0.8:1:0.8:0.6:0.4:0.2 | 4 | 1.0 |
| 13 | 40 | 36 | 3.20 | 0.2:0.4:0.6:0.8:1:0.8:0.6:0.4:0.2 | 10 | 1.0 |
| 14 | 41 | 36 | 3.20 | 0.2:0.4:0.6:0.8:1:0.8:0.6:0.4:0.2 | 10 | 1.0 |
| 15 | 42 | 36 | 3.20 | 0.2:0.4:0.6:0.8:1:0.8:0.6:0.4:0.2 | 10 | 1.0 |
| 16 | 43 | 36 | 3.20 | 0.2:0.4:0.6:0.8:1:0.8:0.6:0.4:0.2 | 10 | 1.0 |
| 17 | 44 | 36 | 3.20 | 0.2:0.4:0.6:0.8:1:0.8:0.6:0.4:0.2 | 10 | 1.0 |
| 18 | 44 | 36 | 3.20 | 0.2:0.4:0.6:0.8:1:0.8:0.6:0.4:0.2 | 10 | 1.0 |
| 19 | 45 | 45 | 3.20 | 0.2:0.4:0.6:0.8:1:0.8:0.6:0.4:0.2 | 10 | 1.0 |
| 20 | 45 | 54 | 3.20 | 0.2:0.4:0.6:0.8:1:0.8:0.6:0.4:0.2 | 10 | 1.0 |
| 21 | 45 | 54 | 3.20 | 0.2:0.4:0.6:0.8:1:0.8:0.6:0.4:0.2 | 50 | 1.0 |
| 22 | 45 | 54 | 3.20 | 0.2:0.4:0.6:0.8:1:0.8:0.6:0.4:0.2 | 100 | 1.0 |
| 23 | 45 | 54 | 3.60 | 0.2:0.4:0.6:0.8:1:0.8:0.6:0.4:0.2 | 100 | 1.0 |
| 24 | 45 | 54 | 3.90 | 0.2:0.4:0.6:0.8:1:0.8:0.6:0.4:0.2 | 100 | 1.0 |
| 25 | 43 | 54 | 3.60 | 0.2:0.4:0.6:0.8:1:0.8:0.6:0.4:0.2 | 80 | 0.5 |
| 26 | 45 | 54 | 3.80 | 0.2:0.4:0.6:0.8:1:0.8:0.6:0.4:0.2 | 100 | 1.0 |
| 27 | 45 | 54 | 3.75 | 0.2:0.4:0.6:0.8:1:0.8:0.6:0.4:0.2 | 100 | 1.0 |
| 28 | 45 | 54 | 3.70 | 0.2:0.4:0.6:0.8:1:0.8:0.6:0.4:0.2 | 80 | 1.0 |
| 29 | 43 | 54 | 3.70 | 0.2:0.4:0.6:0.8:1:0.8:0.6:0.4:0.2 | 80 | 1.0 |
| 30 | 43 | 54 | 3.60 | 0.2:0.4:0.6:0.8:1:0.8:0.6:0.4:0.2 | 80 | 1.0 |
| 31 | 43 | 54 | 3.60 | 0.2:0.4:0.6:0.8:1:0.8:0.6:0.4:0.2 | 20 | 0.5 |
| 32 | 45 | 54 | 3.60 | 0.2:0.4:0.6:0.8:1:0.8:0.6:0.4:0.2 | 50 | 0.5 |
| 33 | 47 | 54 | 3.60 | 0.2:0.4:0.6:0.8:1:0.8:0.6:0.4:0.2 | 50 | 0.5 |
| 34 | 43 | 54 | 3.60 | 0.2:0.4:0.6:0.8:1:0.8:0.6:0.4:0.2 | 50 | 0.5 |
| 35 | 43 | 54 | 3.60 | 0.2:0.4:0.6:0.8:1:0.8:0.6:0.4:0.2 | 40 | 0.5 |
| 36 | 43 | 54 | 3.60 | 0.2:0.4:0.6:0.8:1:0.8:0.6:0.4:0.2 | 60 | 0.5 |
| 37 | 43 | 54 | 3.80 | 0.2:0.4:0.6:0.8:1:0.8:0.6:0.4:0.2 | 80 | 0.5 |
| 38 | 43 | 54 | 4.00 | 0.2:0.4:0.6:0.8:1:0.8:0.6:0.4:0.2 | 100 | 0.5 |
| 39 | 43 | 54 | 4.30 | 0.2:0.4:0.6:0.8:1:0.8:0.6:0.4:0.2 | 100 | 0.5 |
| 40 | 45 | 54 | 4.30 | 0.2:0.4:0.6:0.8:1:0.8:0.6:0.4:0.2 | 100 | 0.5 |
| 41 | 44 | 54 | 4.30 | 0.2:0.4:0.6:0.8:1:0.8:0.6:0.4:0.2 | 100 | 0.5 |
| 42 | 44 | 54 | 4.20 | 0.2:0.4:0.6:0.8:1:0.8:0.6:0.4:0.2 | 100 | 0.5 |
| 43 | 44 | 54 | 4.10 | 0.2:0.4:0.6:0.8:1:0.8:0.6:0.4:0.2 | 90 | 0.5 |
| 44 | 44 | 54 | 4.10 | 0.2:0.4:0.6:0.8:1:0.8:0.6:0.4:0.2 | 90 | 0.5 |
| 45 | 44 | 54 | 4.10 | 0.2:0.4:0.6:0.8:1:0.8:0.6:0.4:0.2 | 95 | 0.5 |
| 46 | 43 | 54 | 4.10 | 0.2:0.4:0.6:0.8:1:0.8:0.6:0.4:0.2 | 95 | 0.5 |
| 47 | 43 | 54 | 4.10 | 0.2:0.4:0.6:0.8:1:0.8:0.6:0.4:0.2 | 93 | 0.5 |
| 48 | 43 | 54 | 4.15 | 0.2:0.4:0.6:0.8:1:0.8:0.6:0.4:0.2 | 100 | 0.5 |
| 49 | 43 | 54 | 4.15 | 0.2:0.4:0.6:0.8:1:0.8:0.6:0.4:0.2 | 97 | 0.5 |

# Bibliography


[1] J. Clarke, P. Neveu, K. E. Khosla, E. Verhagen, and M. R. Vanner,
*Cavity Quantum Optomechanical Nonlinearities and Position Measurement beyond the Breakdown of the Linearized Approximation*, Phys. Rev. Lett. **131** (5 2023) 053601,
URL: https://link.aps.org/doi/10.1103/PhysRevLett.131.053601 (cit. on p. 1).

[2] N. Mavalvala,
*Quantum Optics and Optomechanics: From Fundamental Tests To Quantum Tools of the Future*, NSF Award Number 2308969, Directorate for Mathematical and Physical Sciences, Division of Physics, Accessed via SAO/NASA ADS, 2023,
URL: https://ui.adsabs.harvard.edu/abs/2023nsf....2308969M (cit. on p. 1).

[3] B.-B. Li, L. Ou, Y. Lei, and Y.-C. Liu, Nanophotonics **10** (2021) 2799,
URL: https://doi.org/10.1515/nanoph-2021-0256 (cit. on p. 1).

[4] P. Meystre, *A short walk through quantum optomechanics*, Annalen der Physik **525** (2012) 215,
ISSN: 0003-3804 (cit. on p. 1).

[5] H. Pfeifer et al., *Achievements and Perspectives of Optical Fiber Fabry-Perot Cavities*, (2021),
arXiv: 2111.08533 [quant-ph], URL: https://arxiv.org/abs/2111.08533 (cit. on p. 1).

[6] L. Tenbrake, *Fiber Cavity Optomechanics with Polymer Membranes*,
Master's thesis: Rheinische Friedrich-Wilhelms-Universität Bonn, 2021 (cit. on pp. 1, 4).

[7] D. Stachanow, *Manufacturing Q-optimized polymer-based mechanical resonators for cavity optomechanics with 3D direct laser writing*,
Master's thesis: Rheinische Friedrich-Wilhelms-Universität Bonn, 2024 (cit. on pp. 1, 52).

[8] S. Schmid, L. G. Villanueva, and M. L. Roukes, *Fundamentals of Nanomechanical Resonators*, 2nd ed., Springer Cham, 2023 XII+207, ISBN: 978-3-031-29628-4,
URL: https://doi.org/10.1007/978-3-031-29628-4 (cit. on p. 1).

[9] *IP-S*, Nanoscribe GmbH & Co. KG,
URL: https://support.nanoscribe.com/hc/en-gb/articles/360001750353-IP-S
(visited on 08/21/2025) (cit. on p. 1).

[10] M. Aspelmeyer, T. J. Kippenberg, and F. Marquardt, *Cavity optomechanics*,
Rev. Mod. Phys. **86** (4 2014) 1391,
URL: https://link.aps.org/doi/10.1103/RevModPhys.86.1391 (cit. on p. 1).

[11] A. Ageev, B. C. Palmer, A. D. Felice, S. D. Penn, and P. R. Saulson,
*Very high quality factor measured in annealed fused silica*,
Classical and Quantum Gravity **21** (2004) 3887,
URL: https://dx.doi.org/10.1088/0264-9381/21/16/004 (cit. on p. 1).

[12] J. S. Stein, *Laser-based Micro-Sintering of 3D Direct Laser-Written Optomechanical Resonators*, Bachelor's thesis: Rheinische Friedrich-Wilhelms-Universität Bonn, 2025
(cit. on pp. 1, 3–7, 9, 12, 15, 21).

[13] *GP-Silica*, Nanoscribe GmbH & Co. KG, URL:
https://support.nanoscribe.com/hc/en-gb/articles/360022237999-GP-Silica
(visited on 07/29/2025) (cit. on pp. 1, 6, 9).

[14] M. A. Scharfstädt,
*Implementation of a Micro-Mirror Production Setup for Quantum Information Applications*,
Master's thesis: Rheinische Friedrich-Wilhelms-Universität Bonn, 2022 (cit. on pp. 1, 4, 17).

[15] *3D Microfabrication Solution Set Large Features (3D LF)*, Nanoscribe GmbH & Co. KG,
URL: https://support.nanoscribe.com/hc/en-gb/articles/360017312153-3D-Microfabrication-Solution-Set-Large-Features-3D-LF (visited on 08/03/2025)
(cit. on pp. 3, 19).

[16] H.-B. Sun and S. Kawata,
"Two-Photon Photopolymerization and 3D Lithographic Microfabrication,"
*Advances in Polymer Science*, vol. 170, Berlin, Heidelberg: Springer-Verlag, 2004 169,
ISBN: 978-3-540-20763-6 (cit. on p. 3).

[17] *63x Objective*, Nanoscribe GmbH & Co. KG,
URL: https://support.nanoscribe.com/hc/en-gb/articles/360002471754-63x-Objective (visited on 08/21/2025) (cit. on p. 3).

[18] *Definite Focus (Interface Finder)*, Nanoscribe GmbH & Co. KG,
URL: https://support.nanoscribe.com/hc/en-gb/articles/360003535714-Definite-Focus-Interface-Finder (visited on 08/03/2025) (cit. on p. 3).

[19] L. B. Bezek et al., *Evolution of Debinding and Sintering of a Silica-Based Ceramic Using Vat Photopolymerization Additive Manufacturing*, Preprint / details to be completed, 2025,
URL: https://www.sciencedirect.com/ (cit. on p. 4).

[20] *Printing with the Glass Printing Explorer Set (GP-Silica)*, Nanoscribe GmbH & Co. KG,
URL: https://support.nanoscribe.com/hc/en-gb/articles/4402084033810-Printing-with-the-Glass-Printing-Explorer-Set-GP-Silica (visited on 07/29/2025)
(cit. on pp. 8, 9, 12, 14, 19, 25, 52).

[21] L. Tenbrake, A. Faßbender, S. Hofferberth, S. Linden, and H. Pfeifer,
*Direct laser-written optomechanical membranes in fiber Fabry-Perot cavities*,
Nature Communications **15** (2024) 209,
URL: https://doi.org/10.1038/s41467-023-44490-7 (cit. on p. 21).

[22] *Bubbles (Over-Exposure)*, Nanoscribe GmbH & Co. KG,
URL: https://support.nanoscribe.com/hc/en-gb/articles/360008872953-Bubbles-Over-Exposure (visited on 08/12/2025) (cit. on p. 23).

[23] *3D Printing using Two Photon Polymerization (2PP)*, Nanoscribe GmbH & Co. KG,
URL: https://support.nanoscribe.com/hc/en-gb/articles/360008908273-3D-Printing-using-Two-Photon-Polymerization-2PP (visited on 08/12/2025) (cit. on p. 23).

[24] B. Jung, C. K. Ober, and M. O. Thompson, *Controlled roughness reduction of patterned resist polymers using laser-induced sub-millisecond heating*,
Journal of Materials Chemistry C **2** (2014) 9115,
URL: https://doi.org/10.1039/C4TC01548G (cit. on p. 46).

# Used tools and resources

The following tools and resources and their use for the production of this thesis are listed here;

- ChatGPT-4o was used for grammar and spelling.
- Python was used in a JupyterHub and JupyterNotebook environment for the data analysis.
- Inkscape was used for the production of some of the images.